White matter hyperintensity genetic risk factor *TRIM47* regulates autophagy in brain endothelial cells

ABBREVIATED TITLE: TRIM47 in brain endothelial cells

Sunny Hoi-Sang Yeung[1], Ralph Hon-Sun Lee[1], Gerald Wai-Yeung Cheng[1], Iris Wai-Ting Ma[1], Julia Kofler[2], Candice Kent[3], Fulin Ma[3], Karl Herrup[3], Myriam Fornage[4], Ken Arai[5], Kai-Hei Tse[1#]

[1] Department of Health Technology and Informatics, The Hong Kong Polytechnic University
[2] Division of Neuropathology, School of Medicine, University of Pittsburgh
[3] Department of Neurobiology, School of Medicine, University of Pittsburgh
[4] Human Genetics Center, Division of Epidemiology, School of Public Health, University of Texas Health Science Center at Houston
[5] Neuroprotection Research Laboratory, Departments of Radiology and Neurology, Massachusetts General Hospital, Harvard Medical School

[#] To whom correspondence should be addressed to
Dr. Kai-Hei TSE email: kh-franki.tse@polyu.edu.hk

ABSTRACT

White matter hyperintensity (WMH) is strongly correlated with age-related dementia and hypertension, but its pathogenesis remains obscure. GWAS identified TRIM47 at 17q25 locus as a top genetic risk factor for WMH formation. TRIM family is a class of E3 ubiquitin ligase with pivotal functions in autophagy, which is critical for brain endothelial cell (ECs) remodeling during hypertension. We hypothesize that TRIM47 regulates autophagy and its loss-of-function disturbs cerebrovasculature. Based on transcriptomics and immunohistochemistry, TRIM47 is found selectively expressed by brain ECs in human and mouse, and its transcription is upregulated by artificially-induced autophagy while downregulated in hypertension-like conditions. Using *in silico* simulation, immunocytochemistry and super-resolution microscopy, we identified the highly conserved binding site between TRIM47 and the LIR (LC3-interacting region) motif of LC3B. Importantly, pharmacological autophagy induction increased Trim47 expression on mouse ECs (b.End3) culture, while silencing *Trim47* significantly increased autophagy with ULK1 phosphorylation induction, transcription and vacuole formation. Together, we confirm that TRIM47 is an endogenous inhibitor of autophagy in brain ECs, and such TRIM47-mediated regulation connects genetic and physiological risk factors for WMH formation but warrants further investigation.

SUMMARY STATEMENT

TRIM47, top genetic risk factor for white matter hyperintensity formation, is a negative regulator of autophagy in brain endothelial cells and implicates a novel cellular mechanism for age-related cerebrovascular changes.

KEYWORDS

TRIM family; White matter hyperintensity; *TRIM47*; Brain endothelial cells; Autophagy

Total Word: 6658 (excluding abstract, title page, declarations, methods, and references)
Number of pages: 25
Number of figures: 7
Number of tables: 1 (with 4 supplementary Tables)

DECLARATIONS

Ethics approval and consent to participate

- This study involves human tissue
  - All human tissue experiments from the brain bank in the Neuropathology Core of Alzheimer's Disease Research Center (ADRC) at University of Pittsburgh Medical Center with approvals from the Committee for Oversight of Research and Clinical Training Involving Decedents at University of Pittsburgh. The ADRC is funded by NIH P30 AG066468-02. This cohort of postmortem tissue from the brain bank is ruled as exempt by IRB at University of Pittsburgh Research as it only involves the collection or study of existing data, documents, records, pathological specimens or diagnostic specimens, if these sources are publicly available or if the information is recorded by the investigator and in such a manner that subjects cannot be identified, directly or through identifiers linked to the subjects.
- This study involves animals
  - All animal experiments in this study are approved by Animal Subjects Ethics Sub-committee (ASESC), Research Committee, The Hong Kong Polytechnic University with ASESC reference number 20-21/167-HTI-R-GRF

Consent for publication

- Not applicable

Conflict of interest statement

- The authors declare no competing financial interests.

Availability of data and material

- The datasets during and/or analyzed during the current study available from the corresponding author on reasonable request.

Acknowledgments

- The present work is generously supported by General Research Fund from Research Grant Council (GRF15101422), Hong Kong Special Administrative Region. Dr. Kai-Hei Tse is also supported by PolyU Start-up Fund P0030307. The initial concept of the present work was funded by The Leo and Anne Albert Charitable Trust to Prof. Karl Herrup, Prof. Myriam Fornage, Dr Ken Arai and Dr Kai-Hei Tse
- Prof. Karl Herrup is supported by Start-up Fund at Department of Neurobiology, University of Pittsburgh and the Australian National Health and Medical Research Fund (APP1160691), the Pennsylvania Department of State (4100087331) and additional support from the NIA (R01 AG069912).
- Dr Kofler and Alzheimer's Disease Research Center at the University of Pittsburgh are supported by NIA P30 AG066468 and NIA P50 AG005133.

Authors' contributions

- S.H.S.Y performed cell culture experiments, immunohistochemistry and imaging. R.H.S.L performed image analysis. K.H.T performed RNA-seq meta-analysis and in silico modeling simulations. G.W.Y.C and I.W.T.M. performed animal husbandry. P.H performed the histopathology test. C.K., F.M., K.H., J.K, performed immunohistochemistry on human tissue. S.H.S.Y and K.H.T wrote the first draft of the manuscript. K.H., M.F., K.A., and K.H.T conceptualized the study, designed the experiment, and edited the manuscript. All authors read, critically reviewed, and approved the manuscript. K.H.T supervised the study and obtained funding.

INTRODUCTION

White matter hyperintensities (WMH) are abnormally strong signals detectable by magnetic resonance imaging (MRI) commonly found in the aging brain. The intense signals of WMH are the likely consequence of cerebrovascular changes with freely diffusible fluid originated from a leaky blood brain barrier (BBB), microbleeds (Alber et al., 2019; Roseborough et al., 2023). The age-related WMH burden increases with age and is significantly associated with cognitive decline (Au et al., 2006; Brown et al., 2021; Habes et al., 2016; Prins and Scheltens, 2015; Vergoossen et al., 2021). The radio-pathological correlation studies of WMH regions revealed a range of neuropathology including microinfarcts, astrogliosis, microglia activation, arteriolosclerosis and myelin loss (Fazekas et al., 1993; Gouw et al., 2008; Kalaria, 2016; Shim et al., 2015). The most consistent is BBB leakage as evident by the detection of fibrinogen in the penumbra region (Bridges et al., 2014; Hainsworth et al., 2017). At the WMH site, the cerebral capillary dysfunction triggers blood flow reduction, BBB disruption followed by fibrinogen breaching which ultimately causes oligodendrocyte loss (Montagne et al., 2018). While the gradual myelin loss would lead to cognitive impairment in age-related dementia (Tse and Herrup, 2017), the initial mechanism triggering the cerebrovascular changes underlying the WMH formation remains elusive.

Hypertension is one of the most prevalent conditions in the aging population, and it is the major risk factor for WMH formation (Chesebro et al., 2020; Hajjar et al., 2011; Verhaaren et al., 2013). The chronic hardening and narrowing of blood vessels in the cerebrovasculature can drive WMH-associated cognitive impairment even in young and asymptomatic populations (Hasan-Olive et al., 2019; Maillard et al., 2012). Cerebrovasculature is a highly dynamic system, whose flexibility is conferred by the constituent endothelial cells (ECs) (Kim et al., 2018). Together with pericytes and astrocytes, EC is one of the three cellular constituents of BBB, and it forms the interface between blood and brain (Zhao et al., 2015). At the vascular lumen, ECs constantly encounter shear stress of blood flow and adapt to hemodynamics by remodeling themselves through autophagy (De Meyer et al., 2015; Nussenzweig et al., 2015). In hypertensive conditions, the vascular tone and blood flow in the cerebrovasculature are impaired (Pires et al., 2013), and likely lead to autophagy failure in ECs (Vion et al., 2017). As the restoration of autophagy was shown to reduce hypertension associated cerebrovascular dysfunction (Forte et al., 2020), we propose that impaired autophagy in ECs may be the underlying cause of hypertension-driven BBB leakage and WMH formation.

Despite the strong link between hypertension, autophagy failure and BBB leakage, not every hypertensive patient develops WMH (Hajjar et al., 2011). Population genetics fill this gap of knowledge. Independent GWAS (Genome wide association studies) identified SNPs (single nucleotide polymorphism) that confer significant risk to WMH development in the healthy aging population at locus at 17q25 (Fornage et al., 2011; Persyn et al., 2020; Sargurupremraj et al., 2020; Sarnowski et al., 2018; Traylor et al., 2019; Verhaaren et al., 2015). Among the six genes (*WBP2, TRIM65, TRIM47, MRPL38, FBF1,* and *ACOX1*) found at this locus, two are members of tripartite motif (TRIM) family. Importantly, a recent study combining GWAS and whole exome sequencing mapped to a missense variant of *TRIM47* that may cause the damaging effects towards WMH formation (Mishra et al., 2022). TRIM is a large family of E3 ubiquitin ligases with more than 80 members in the human genome. Members of TRIM family regulate protein turnover, quality control and degradation through ubiquitin-proteasome system during development, immunity and carcinogenesis (Hatakeyama, 2017). Surprisingly, TRIM family members are also heavily involved in the regulation of autophagy.

Many TRIM members were experimentally verified to interact with key autophagic adaptors including LC3, SQSTM1/p62 or ULK1/Beclin. Together, the proteins form a TRIM-containing complex during autophagosome formation for macroautophagy (Mandell et al., 2014), as well as selective microautophagy to precisely degrade intracellular organelles (Kimura et al., 2016). For example, TRIM65 is known to facilitate autophagy by controlling Atg7 expression in cancer cells (Pan et al., 2019). Yet, the role of TRIM47 in autophagy remains unknown, especially in endothelium. With the strong population genetic evidence, we hypothesized that the dysfunction of TRIM47 may cause autophagy failure in brain ECs, followed by BBB disintegration and WMH formation. In this study, we aim to characterize the role

of TRIM47 in EC autophagy using a series of bioinformatic analysis coupled with experiments *in silico* and *in vitro.*

METHODS

Query of gene expression omnibus repository and scRNA-seq

The Gene Expression Omnibus (GEO) repository of NCBI was queried for datasets targeting hypertension, autophagy and/or endothelial cells. Four datasets (GSE108384, GSE199709, GSE180169 and GSE131712) were identified to test our hypothesis that *TRIM47* expression is altered in endothelial cells in hypertensive environments. The exploration and re-analysis were performed on the GEO2R R-based web application (Barrett et al., 2013) and GREIN:GEO RNA-seq Experiments Interactive Navigator (Mahi et al., 2019). The differential gene expression signature obtained in the pairwise comparison was identified. The significantly upregulated or downregulated genes reaching a false discovery rate or an adjusted P-value < 0.05 were then curated for gene ontology (GO) enrichment analysis by PANTHER-based platform (Mi et al., 2019).

In silico analysis of TRIM47

To screen for the LC3-interacting region (LIR) motif among, the protein sequences of TRIM family members were queried in iLIR database, a web-based search engine LIR motif-containing proteins in eukaryotes (Jacomin et al., 2016; Kalvari et al., 2014). To simulate the three dimensional structure, the protein sequence of TRIM47 was mapped using Phyre2 server as described (Kelley et al., 2015). The best fit model generated by Phyre2, as well as the human and mouse TRIM47 protein model predicted by Alphafold artificial intelligence algorithm (Jumper et al., 2021) were docked with the human (PDB: 3VTU) or mouse LC3B (Alphafold: Q8C0E3) models using ClusPro web server 2.0 (Kozakov et al., 2017). The computed binding affinity between the protein structures were sorted based on scores measured by the estimated free energy coefficient ($E_{balanced}$) and the binding cluster size. The best ranked protein-protein interaction structures were then explored, annotated and analyzed for contact area using software ICM Browser Pro (Molsoft L.L.C, (Abagyan et al., 1994)).

Postmortem human brain tissue

A cohort of formalin fixed paraffin embedded (FFPE) postmortem brain tissues were used were kindly provided by the Neuropathology Core of Alzheimer's Disease Research Center at University of Pittsburgh Medical Center with approvals from the Committee for Oversight of Research and Clinical Training Involving Decedents at University of Pittsburgh. The postmortem tissues were of frontal cortex origin (Brodmann area 9) from two males and seven females of Alzheimer's disease (AD, Braak Stage VI) and age-matched controls (Braak Stage 0-III) between the ages of 73 and 90 years old. The postmortem interval was between 3.5 and 19 hours. All tissues were sectioned at 12 µm and stored at room temperature until use.

Animal study

The animal experiment was approved by the Animal Subjects Ethics Sub-Committee at The Hong Kong Polytechnic University (PolyU) (ASESC Case No.: 20-21/167-HTI-R-GRF) with a valid license from the Department of Health in Hong Kong. Wildtype mice (WT, C57BL/6J) were housed in individually ventilated cages (Techniplast, Italy) in a temperature and humidity-controlled environment with food (PicoLab Diet 5053, LabDiet Inc, MO, USA) and water *ad libitum* on a 12-hour light/dark cycle The brain tissue was extracted from WT mice at ten months of age (n = 3). Briefly, animals were deeply anesthetized prior to transcardial perfusion with phosphate buffer saline, as described earlier (Mok et al., 2023). The fresh brain was fixed by paraformaldehyde (4%, 24 hours) and then cryoprotected in PBS-sucrose (30% w/v, 72 hours) at 4 °C before embedded for cryosectioning on SuperFrost-plus slides at 10 µm thickness.

Immunohistochemistry-Immunofluorescence

For human tissue, the paraffin-fixed sections were dewaxed with xylene before rehydration in a series of ethanol/phosphate-buffered saline. The rehydrated sections were antigen retrieved with citrate buffer (pH 6.0) at 95°C for 10 min. After cooling and rinsing, the non-specific antibody binding was then blocked using 10% donkey serum at room temperature for one hour, followed by overnight incubation at 4°C with the primary antibody against TRIM47 (1:100, rabbit polyclonal, ab72234, Abcam). The tissue sections were washed and then incubated in AlexaFluor-conjugated secondary antibody for 1 h at room temperature with nuclear counterstained by PI. All immunofluorescence image of the human tissues was captured in University of Pittsburgh using a Nikon A1R confocal system based on an Eclipse Ti2 microscope equipped by a 20x (Nikon N Plan Apo 20x/0.75), 40x (Nikon N Plan Apo 40x/0.95) dry objectives, or 60× (1.4 Numerical Aperture) oil objective lens and a camera (at 512 µm × 512 µm) operated by NIS-Elements AR software. Three Region-Of-Interests were captured per specimen for quantification.

For mouse tissue, the frozen sections were washed and blocked with normal donkey serum (10% v/v) in phosphate buffer saline (PBS) with 0.3% Triton X-100 for 1 hour at room temperature. Then blocked tissues were then incubated with specific primary antibodies against anti-CD31 antibody [P2B1] ab24590 (1:500, mouse monoclonal, ab72234, Abcam) and anti-TRIM47 (1:500, rabbit polyclonal, ab72234, Abcam) overnight at 4 °C. The sections were then washed with PBS before incubation with incubated secondary antibodies against mouse or rabbit IgG conjugated with Alexa Fluor 488 or 555 or 647 (Thermo Fisher Scientific, MA) for one hour at room temperature. All nuclei were counterstained with DAPI before mounting in Hydromount (National Diagnostics, GA, USA) with coverslips. Whole brain tissue sections were taken by a Nikon Eclipse Ti2-E Live-cell Fluorescence Imaging System at University Research Facility in Life Sciences as described below. The image was analyzed by ImageJ (FIJI 1.53, National Institute of Health, MD, USA).

Cell culture study

To study the function of Trim47 in autophagy, an endothelial cell line derived from mouse brain, bEnd.3 (CCL-2299, ATCC), was used (Montesano et al., 1990). bEnd.3 cells were maintained in complete Dulbecco's Modified Eagle Medium supplemented with 10% (v/v) fetal bovine serum and 1% (v/v) and penicillin/streptomycin mixture in incubator at 37ºC with 5% CO_2. To passage, the cells were detached with 0.25% (v/v) trypsin before replating. To study autophagy, bEnd.3 cells were treated with either 3-methyladenine (3-MA, #1292 Tocris, MN, USA) or rapamycin (Rapa, #3977 Tocris, MN, USA) for 24 hours, or gene silencing described below, before downstream analysis.

Gene silencing

To study the loss-of-function, *Trim47* expression in bEnd.3 cells was silenced by SMARTpool siRNA (siGENOME Mouse Trim47, Gene ID 217333, M-056879-01-0020) or control siRNA (siGENOME non-targeting, D-001206-13-20) using DharmaFECT 1 Transfection Reagent (T-2001-02, Horizon Discovery, USA) according to manufacturer's instruction.

Western blotting

To obtain cell lysates, the cells were lysed by in radioimmunoprecipitation assay buffer (20-188, Millipore, CA, USA) with protease and phosphatase inhibitors (Roche, Hong Kong). After quantification, the protein samples were normalized (Bio-Rad Protein Assay, 5000001, Bio-Rad, CA, USA) and 30 µg were loaded into a 7.5 to 12% sodium dodecyl sulfate (SDS)-polyacrylamide gel for electrophoresis. For the routine immunoblotting, the protein was heated for 5 minutes at 95ºC for denaturation. For non-denaturing immunoblotting, the heating step was omitted and the SDS was omitted from the sample buffer. The resolved proteins were transferred to a semi-dry polyvinylidene difluoride (PVDF) membrane using Bio-Rad Trans-Blot Turbo Transfer System (1704150, Bio-Rad, CA, USA). After blocking non-specific bindings with 5% non-fat milk, the blot was probed against TRIM47 (1:500, rabbit polyclonal, ab72234, Abcam), LC3B (1:1000, E5Q2K, mouse monoclonal #83506, Cell signaling technology/CST), ULK1 (1:1000, D8H5, rabbit monoclonal #8054S, CST), p-ULK (Ser555) (1:1000, D1H4, rabbit monoclonal,

254 #5869, CST), p62 (1:1000, D1Q5S, rabbit monoclonal, #39749, CST), p-p62 (Ser349) (1:1000, E7M1A,
255 rabbit monoclonal, #16177, CST) and GABARAP (1:1000, E1J4E, rabbit monoclonal, #13733, CST). After
256 overnight incubation, the probed blots were incubated with horseradish peroxidase-conjugated secondary
257 immunoglobulins (Cell Signaling Technology, MA, USA). After washes with tris-buffer saline-Tween, the
258 protein signals were captured by chemiluminescent substrates (SuperSignal™ West Pico or Extended Dura
259 or Femto Maximum Sensitivity Substrate, Thermo Fisher Scientific, MA, USA) and the blot image was
260 acquired using Bio-Rad ChemiDoc MP Imaging System (12003154, Bio-Rad, CA, USA) with a continuous
261 exposure for 5 minutes. To quantify the protein expression level, the density and the size in kilodalton (kDa)
262 of each individual band was measured by ImageJ (FIJI, v1.53, National Institute of Health, MD, USA).
263
264 *Gene expression*
265 The total RNA was isolated from the cells using RNeasy Mini Kit (Qiagen, Germany, 74106). Any
266 remaining genomic DNA in the RNA sample was digested by DNase I (1 Unit /µL, Thermo Fisher
267 Scientific, MA, USA). To generate cDNA, reverse transcription was performed with High-capacity RNA-
268 to-cDNA kit (Applied Biosystem, Thermo Fisher Scientific, MA, USA). The genes of interest and the
269 housekeeping gene, *Gapdh*, was amplified and analysed in real-time polymerase chain reaction on a Roche
270 Light Cycler 480 system with TB Green® Premix Ex Taq™ II (TaKaRa Bio Inc., Japan). The specific
271 primers were predesigned and validated by PrimerBank of Massachusetts General Hospital (Spandidos et
272 al., 2010), with the primer sequences detailed in Table S1.
273
274 *Immunocytochemistry*
275 For microscopic examination, immunocytochemistry was performed as described (Mok et al.,
276 2023). The bEnd.3 cells plated on coverslips were fixed by 4% paraformaldehyde (pH 7.2) for 30 minutes.
277 After washing with PBS, the potential non-specific binding was blocked with 5% (v/v) normal donkey
278 serum (D9663, Sigma-Aldrich) in PBS containing 0.3% Triton X-100 for 30 minutes at room temperature.
279 The specimen was then incubated with primary antibody against LC3B (83506S, 1:400, Cell Signaling
280 Technology) as well as TRIM-47 (ab72234, 1:400, Abcam), p-p62 Ser349 (1:800, CST, #16177S), p-ULK1
281 Ser555 (1:250, CST, #5869) or GABARAP (1:200, CST, #13733) for two hours, followed by fluorescent
282 visualization with donkey anti-mouse or anti-rabbit Alexa fluor-488 or -555 (A31572, A21202, Thermo
283 Fisher Scientific, MA, USA). The stained coverslip was further incubated with DAPI (4',6-diamidino-2-
284 phenylindole, 1 µg/mL) for 5 minutes before mounted on glass slide with Hydromount aqueous mounting
285 medium (HS106100ML, National Diagnostics). The coverslips were examined with a Nikon Eclipse Ti2-
286 E Live-cell Fluorescence Imaging System at University Research Facility in Life Sciences. The system is
287 equipped with DS-Qi2 monochrome camera and a multi-wavelength LED illumination system (CoolLED
288 pE-4000) with blue (Ex: 380/55), green (Ex: 470/30), red (Ex: 557/35) and far-red (Ex: 620/60) filters with
289 a Nikon Plan Apo λ 20x Objective (N.A. 0.75, R.I. 1.0). Duplicate coverslips were included for each
290 condition and a total of five images (2424 x 2424 pixel) from random fields (882.5 µm x 882.5 µm) was
291 acquired using Nikon NIS elements software, (V5.21.03 Nikon Instruments, NY, USA). Image analysis
292 was performed by QuPath (Bankhead et al., 2017) and Cellprofiler (McQuin et al., 2018).
293
294 *Quantification of autophagic punta*
295 The quantification of ATG8 punta is a standard approach to measure the level of autophagic flux
296 (Klionsky et al., 2021). To quantify autophagy, the immunocytochemistry image was analyzed by the open-
297 source CellProfiler Software of version 4.2.5 (McQuin et al., 2018). Briefly, the triple immunofluorescent
298 images (2424x2424 pixels at 0.36 µm/pixel) were separated into three channels and converted into
299 greyscale. The primary objects of the nucleus, green or red punta were identified and related in each cell.
300 The related features were then classified, filtered and masked for the measurement of signal colocalization.
301 In each masked cell, the second and tertiary objects segmenting the cytoplasm and the cytoplasmic punta
302 were then identified and classified, with the number of cytoplasmic punta in each positive cell quantified
303 for analysis.
304

Structured Illumination Microscopy imaging

Super resolution microscopy was performed using a Structured Illumination Microscopy (SIM) system at University Research Facility in Life Sciences. The Nikon N-SIM was built on a fully motorized Eclipse Ti inverted microscope body equipped with Nikon LU-NV MultiLaser (TIRF), ORCA-Flash4.0 V2+ sCMOS camera and CFI SR HP Plan Apo 100× (NA = 1.35) oil objective lens. The XY resolution is 115 nm and Z resolution is 250 nm in SIM mode (Nikon Instruments, NY, USA). To prepare the samples for N-SIM, cells were plated on 1.5H 13 mm Marienfeld no. round coverglass as described above but with the specimen mounted using ProLong Diamond antifade mountant (Thermo Fisher Scientific, MA, USA). The acquired datasets with an array of 1024 × 1024 pixels across the Z steps of 1 micron were computationally reconstructed using built-in algorithm in NIS-Elements AR software.

Statistics

For each experiment, at least three independent biological replicates were included, and the total number of experiments is denoted as *n* number in each graph. A Grubbs' test was performed for outliners identification. For comparisons of one variable between two groups, an unpaired t-test was performed. For comparisons of one variable in more than two groups, a one-way analysis of variance (ANOVA) was performed with a post-hoc test for multiple comparison. For comparisons of two or more variables in more two groups or above, a two-way ANOVA with a post-hoc multiple comparison was conducted. All statistical analyses were performed using GraphPad Prism software version 10.0 (GraphPad Software Inc. MA, USA). All statistical analyses were two-tailed with, and the significance level was set at $p < 0.05$. The details of the analysis and post-hoc tests are stated in each figure legend.

RESULTS

To test our hypothesis that TRIM47 dysfunction in the brain endothelium leads to WMH formation, we first seek to confirm if *TRIM47* is selectively expressed in brain EC. To test, we prompted multiple single cell RNAseq (scRNAseq) database libraries of human and mouse brain tissues using the single cell portal (Fig. 1). In two independent scRNAseq libraries of human prefrontal cortices from healthy adult subjects (males, n =5 (Habib et al., 2017); female, n = 1 (Russell et al., 2023)), *TRIM47* expression was highly enriched in the brain ECs and astrocytes and essentially absent in other brain cell types, including neurons (Fig. 1A). Further exploration of an additional scRNAseq library of normal human blood brain barriers further showed that brain ECs from arterioles, capillaries and veins similarly express TRIM47 and their level is stronger than that of pericytes and fibroblast (Fig. 1B, C, (Garcia et al., 2022)), while the level in smooth muscle cells was highly variable. Using immunohistochemistry on a cohort of healthy and AD human cerebral cortex, we confirmed that TRIM47 signals are detectable in the endothelium of the capillary and arteriole-like structures (Fig.1D), but not in neuron or neurophil. To confirm *Trim47* expression pattern in mouse brain, we explored the scRNAseq library of mouse whole brain (C57BL/6J, 2-3 months of age, n = 8, (Ximerakis et al., 2019)) and a scRNAseq library of mouse whole cerebral cortex (C57BL/6J, 1 month of age, n = 1, (Ding et al., 2020)). We found that *Trim47* is strongly expressed by mouse brain ECs in these independent libraries (Fig. 1E). This is confirmed by an additional query on a third library of scRNAseq of transcriptions from nine adult mouse brain regions (i.e. frontal cortex, posterior cortex, substantia nigra, striatum, thalamus, globus pallidus, entopeduncular, hippocampus and cerebellum; C57Blk6/N, 2 months of age). In each brain region, the highest level of *Trim47* transcription was found in the Fit1$^+$ ECs population (Fig. 1F, http://dropviz.org/ (Saunders et al., 2018)). In both datasets, pericytes also express Trim47 at a lower level. Using immunohistochemistry, we confirmed that Trim47 is selectively expressed by CD31$^+$ brain endothelial cells in wildtype C57BL/6J mice at 10 months old (Fig. 1G). These observations from six independent scRNAseq datasets agree with our histology experiments and suggest that TRIM47 is selectively expressed by brain ECs of human and mouse.

We then characterized *TRIM47* expression in ECs during autophagy and autophagy-inducing conditions through a meta-analysis of TRIM family members in independent RNA-seq datasets. First, in

354 adenovirus-mediated TFEB (transcription factor EB, the master regulator of autophagy) overexpression in
355 primary human EC culture (HUVEC, human umbilical vein endothelial cells), autophagy was significantly
356 induced with increased EC migration and tube formation (Fan et al., 2018) (Table S2 and Table S3). The
357 meta-analysis of the microarray dataset (GSE108384) showed that 27 *TRIM* family members were
358 significantly and differentially expressed in these autophagic human ECs (adjusted P value < 0.05). Among
359 the differentially expressed *TRIM* members, *TRIM47* was the third most upregulated gene (Log_2 fold change
360 = 1.16, Fig. 2A). It is proposed that ECs undergo autophagy to remodel the vascular structure upon
361 stimulation by luminal shear stress (De Meyer et al., 2015; Nussenzweig et al., 2015). To test our hypothesis
362 that TRIM47 function may be associated with such blood flow-related autophagy, we inquired *TRIM* family
363 members expression in a human aortic ECs model with or without luminal shear stress simulation (12
364 dyn/cm^2, 12 hours; RNA-seq, GSE199709) (Meng et al., 2022). In gene ontology analysis, macroautophagy
365 (GO:0034262) was significantly enriched by the differentially upregulated genes expressed by ECs
366 immediately after 12 hours shear stress treatment (Table S3). In this autophagic condition, 14 out of the 49
367 detectable *TRIM* family members were significantly and differentially expressed by the ECs, where
368 *TRIM47* was the sixth most significantly downregulated family member (Log_2 fold change = -0.41, Fig.
369 2B), but such reduction was abolished after 24 hours of recovery in static medium (Table S3).

370 To confirm if the association between *TRIM47* and autophagy is conserved in the mouse model,
371 we investigated *Trim47* expression in a pulmonary hypertension model (PAH, (Rodor et al., 2022)). The
372 lung ECs in the PAH model were sorted by flow cytometry, and we identified a significant enrichment of
373 the autophagic process in the hypertensive condition, as in humans (Fig. 4C and Table S3). Among the 49
374 detectable *Trim* family members, three were significantly downregulated in the ECs and *Trim47* ranked
375 number one (Log_2 fold change = 1.85, RNA-seq, GSE180169). As changes in blood flow of the
376 cerebrovasculature will cause autophagy failure in brain ECs (Pires et al., 2013; Vion et al., 2017), we
377 inquired if *Trim47* expression is altered in an ischemic brain injury model. In a mouse model of transient
378 middle cerebral artery occlusion (MCAO, C57BL/6J, 8–10 weeks of age, occlusion for 1 hour, (Wu et al.,
379 2019)), 14 out of the 59 detectable *Trim* family members were significantly and differentially expressed in
380 the ipsilateral cerebral cortex 24 hours post-injury, where *Trim47* was the most significantly downregulated
381 member (Log_2 fold change = -3.163, RNA-seq, GSE131712). Intriguingly, such downregulation was
382 abolished after 28 days of recovery in the ipsilateral cortex. In a similar mouse MCAO model (129S6/SvEv,
383 8-10 weeks of age, occlusion for 30 minutes, (Wegner et al., 2020)), the brain ECs isolated from the injured
384 brain after 72 hours of recovery similarly showed no changes in any *Trim* family members and no
385 autophagic process was significantly enriched among the differentially expressed genes (FDR-based, RNA-
386 seq, GSE122345, Table S2 and S3). Together, these independent datasets suggested the TRIM47
387 transcription in ECs is significantly upregulated when autophagy is artificially induced, but significantly
388 downregulated when the hypertension- or cerebrovascular dysfunction-related autophagy begins.

389 The bioinformatic inquiry above suggested that TRIM47 belongs to the group of TRIM family
390 members not only involved in ubiquitination-mediated degradation, but also in autophagy. Indeed, many
391 of TRIM members interacts with human ATG8 (LC3), p62/SQSTM1 and/or ULK1/Beclin1 (TRIM -1, -5,
392 -6, -13, -16, -17, -20, -21, -22, -28, -33, -40, -41, -45, -49, -50, -55, -61, -63 and -76) (Hatakeyama, 2017;
393 Mandell et al., 2014) and forms a TRIM-containing complex during autophagosome formation.
394 Nevertheless, TRIM47 was not detected as one of these autophagic regulating members. To clarify, we
395 performed a systemic screening of human and mouse TRIM protein sequences for the LIR motifs using
396 iLIR database (Table 1) (Jacomin et al., 2016; Kalvari et al., 2014). LIR motif is the consensus amino acid
397 sequence responsible for autophagic functions. This consensus sequence includes WxxL and xLIR, where
398 **W**xx**L** is the canonical consensus sequence of LC3B interacting site where x can be any amino acid among
399 the four residues. The consensus was then extended as xLIR, where the six amino acid residues can be any
400 combination of (ADEFGLPRSK)(DEGMSTV)(**WFY**)(DEILQTV)(ADEFHIKLMPSTV)(**ILV**). Such
401 motif would also have a higher probability to bind to LC3 if it is located within an anchor, a disordered
402 region with high potential to be stabilized upon binding (Kalvari et al., 2014). Using the position specific

403 scoring matrix (PSSM) as the measurement, we found that human TRIM47 attained a PSSM score of 14
404 and it is within the threshold range of the verified xLIR molecules (PSSM = 13-17) (Kalvari et al., 2014).
405 Importantly, the xLIR (NQWEQL) motif in human TRIM47 fit within an anchor region. Such potential
406 LC3 interacting site was conserved in mouse Trim47 (SQWEQL). Although this motif is not embedded
407 within an anchor, the xLIR in Trim47 attained a PSSM score of 16 and within the threshold of verified
408 xLIR containing proteins. Intriguingly, a low PSSM score was found in human TRIM65 (9) and mouse
409 Trim65 (8), the other TRIM family member identified in the 17q25 locus.
410
411 To confirm the putative autophagic function of TRIM47, we performed a structural analysis of the
412 potential TRIM47-LC3B interactions *in silico*. As no prior X-ray crystallography-based or NMR-based
413 study is available, we first predicted the protein folding structure of human TRIM47 using Phyre2 Protein
414 Fold Recognition Server (Kelley et al., 2015). Under the intensive mode of simulation, the final TRIM47
415 model mapped on the templates of TRIM20 (PDB: 4CG4; Sequence identity 16%, Confidence 100%),
416 TRIM25 (PDB: 6FLN; Sequence identity 24%, Confidence 100%) and TRIM28 (PDB: 6QAJ; Sequence
417 identity 19%, Confidence 100%), see Fig 3A-C. This model was docked with human LC3B protein in
418 ClusPro server (Kozakov et al., 2017), and we identified the potential interactions between the TRIM47
419 xLIR motif (N379 and Q380 of NQWEQL) and LC3B (K55 and R14, PDB: 3VTU) with a distance of 2.7
420 – 2.9 Å (Table S4). To validate this interaction, we repeated the LC3B docking experiment with a new
421 artificial intelligence based human TRIM47 model predicted by Alphafold (Jumper et al., 2021) (Alphafold:
422 Q96LD4. Fig. 3D-F). In this docking experiment, we similarly identified potential interactions between the
423 TRIM47 xLIR motif and LC3B, but through different residues, where the W381, Q383 and L384 of
424 NQWEQL bound to I21, R72 and V93 of LC3B (PDB: 3VTU) with a distance between 2.3 – 4.1 Å.
425 Importantly, the putative NQWEQL interacting contacts at R14 and R72 are identical to the known LC3B
426 binding site at hydrophobic pocket 1 and 2 (HP1 near helix α1, HP2 near helix α3; equivalent to residue
427 R10 and R69 of PDB: 5WRD, respectively (Wirth et al., 2019)). Furthermore, the K55 contact site is also
428 a known basic residue and electrostatic binding site important for p62/SQSTM1-LC3 interactions
429 (equivalent to residue K50; (Johansen and Lamark, 2011)). To test if Trim47-LC3B interaction is conserved
430 in mouse, we docked mouse Trim47 (Alphafold: Q8C0E3) and mouse LC3B (Alphafold: Q9CQV6) and
431 identified a similar binding as in human (Fig 3G-I). Although the binding residues between the mouse xLIR
432 in Trim47 (SQWEQL) and LC3 at F80 and M88 were not known sites of interaction important for
433 autophagy, the potential interaction (Energy weighted score) is comparable to that in human (See Table
434 S4). Together, this docking simulation confirms that TRIM47 interacts with LC3B in human and mouse.
435
436 The bioinformatic and *in silico* analysis thus far suggested that TRIM47 is selectively expressed
437 by ECs in the brain and is a plausible partner of LC3B during autophagic conditions. We experimentally
438 tested these findings on a murine brain-derived endothelial cell line, bEnd.3, using a pharmacological
439 approach. By applying 3-methyladenine (3-MA; 0, 0.1, 1 mM) and rapamycin (Rapa, 0, 20, 200 nM) in full
440 medium for 24 h, we modulated autophagy inhibition and activation on bEnd.3, respectively (Cheng et al.,
441 2020; Wu et al., 2010). At transcription level, 3-MA and Rapa induced differential expression of autophagy
442 genes only at the low concentration, such as *Ulk1*, *Ulk2*, *Map1c3b* (LC3B), *Sqstm1* (p62) and *Gabarap*
443 (Fig. 4A, B). At low concentration, Rapa increased *Trim47* transcription but did not reach statistical
444 significance while 3-MA had no effects. Of note, 3-MA slightly induced autophagy at high concentrations,
445 and it was likely due to the role of 3-MA as autophagy activator at high dose in the presence of complete
446 medium (Wu et al., 2010). Immunoblotting showed that Rapa (200 nM) induced a significant increase of
447 LC3B II/LC3B I conversion indicative of autophagy, and such induction was associated with a decrease of
448 Trim47 (Fig. 4C).
449
450 To visualize the Trim47 expression in association with different stages of autophagy, the treated
451 cells were examined for LC3B colocalization with p-ULK1^{Ser555}, p-p62^{Ser349}, GABARAP and Trim47,
452 respectively (Fig. 4D-H). LC3B is the ATG8 member that serves as the marker of autophagy process. The
453 phosphorylation of ULK at serine 555 is mediated by AMPK and is a critical for starvation-induced

454 autophagy at the initiation stage (Egan et al., 2015). The phosphorylation of p62/SQSTM1 at serine 349 is
455 induced selective autophagy (Ichimura et al., 2013). GABARAP is an ATG8 member that is known to
456 associate with LC3B that regulates ULK1 activity in autophagosome formation in response to starvation
457 (Grunwald et al., 2020). The inhibition and promotion of autophagy by 3-MA and Rapa did not alter the
458 overall percentage of LC3B^{+} bEnd.3 cells, but quantifications showed that the two compounds mediated
459 opposing effects on cytoplasmic LC3B punta count per field ($P < 0.05$, Fig. 4D). Further quantifications of
460 p-ULK1$^{Ser555+}$ cells showed that the percentage of bEnd.3 at initiation stage was significantly reduced by 3-
461 MA (by 10.1%, 0.1 mM, $P < 0.05$) but increased by Rapa (by 14%, 20 nM, $P < 0.01$, Fig. 4I). A 2.3-fold
462 difference in LC3B-p-ULK1^{Ser555} double positive cells was found between 3-MA and Rapa treatment,
463 suggesting differential levels of autophagy induction, as expected (Fig. 4J). In these conditions, the number
464 of p-p62^{Ser349} positive and LC3B-p-p62^{Ser349} double positive bEnd.3 cells remained unchanged, suggestive
465 of minimal selective autophagy. The bEnd.3 cells expressing GABARAP, an ATG8 family member that
466 mediates opposing function against LC3 (Grunwald et al., 2020), was significantly lowered by Rapa
467 compared with 3-MA (20%, $P < 0.01$). Finally, immunocytochemistry showed that Trim47 expression
468 appeared as punta and was localized both in the cytoplasm and nucleus (Fig. 4H and Fig. 5). While
469 autophagy inhibition by 3-MA increased Trim47^{+} bEnd.3 cells by 15.3% (vs control, autophagy activation
470 by Rapa reduced Trim47^{+} bEnd.3 cells by 36.1% (vs control, $P < 0.05$) (Fig. 4I). Of note, the significant
471 difference in Trim47^{+} bEnd.3 cell numbers between 3-MA and Rapa treatments appeared as an opposing
472 trend to p-ULK1^{Ser555} induction. The reduction of Trim47 monomer (70 kDa) by low concentration of Rapa
473 (20 nM), but not 3-MA (0.1 mM), found in the immunocytochemistry was confirmed by immunoblotting
474 (Fig. 4K). As the colocalization between Trim47 and LC3B (Fig. 4D) was highly comparable to that
475 between GABARAP and LC3B (Fig. 4F), and such Trim47^{+} LC3B^{+} double positive cells were significantly
476 reduced after Rapa treatment (Fig. 4G), these data suggested that Trim47 is closely associated with LC3B
477 as predicted by the *in silico* model and it may be a negative regulator of autophagy.
478
479 Many TRIM members were experimentally verified to interact with key autophagic adaptors
480 including LC3 (i.e *TRIM5, -17, -20, -21, -22, -28, -41, -49, -55*) or SQSTM1/p62 (i.e *TRIM5, -13, -17, -21,*
481 *-22, -28, -49, -50, -55, -63*) and they form TRIM-containing complex during autophagosome formation
482 (Mandell et al., 2014), which serve as platform for macroautophagy and selective autophagy (Kimura et al.,
483 2016). To examine such potential interactions, we examined the punta colocalization between LC3B with
484 known adaptors including p-ULK1 (p-ULK1^{Ser555}) p62 (p-p62^{Ser349}), GABRARAP and Trim47 in bEnd.3
485 cells with or without 3-MA or Rapa treatment (Fig. 5). The increased p-ULK1^{+} cells were associated with
486 an increase of p-ULK1^{+} cytoplasmic punta (Fig. 5A, B). Although the number of p-p62^{+} cell remain
487 unchanged, the p-p62 and p-p62-LC3B^{+} double positive punta per cell was significantly increased by Rapa
488 ($P < 0.05$, Fig. 5C, D). For GABARAP, a known ATG8 member and an LC3B partner, the average number
489 of GABARAP^{+} and GABARAP^{+}LC3B^{+} punta in each positive cell remained unchanged by 3-MA and Rapa
490 treatment (Fig. 5E, F). Finally, a clear colocalization between Trim47^{+} and LC3B punta was identified (Fig.
491 5G, H). Importantly, although the cell number of Trim47^{+} LC3B^{+} b.End3 was significantly reduced by Rapa
492 (Fig. 4J), the number of Trim47^{+} and Trim47^{+}LC3B^{+} punta in the persisting Trim47-expressing bEnd.3
493 cells were doubled by Rapa treatment (Fig. 5F). Using SIM-based super-resolution microscopy (Fig. 5I-L),
494 we confirmed the close proximity between LC3B and Trim47 in control conditions (Fig. 5I) with their
495 colocalization at a resolution < 200 nm in Rapa-mediated autophagy (Fig. 5K).

496 The downregulation of *Trim47* autophagic conditions of ECs and the reduction of Trim47-
497 expressing cells upon Rapa treatment suggested that Trim47 may be negatively correlated with autophagy.
498 We proposed that TRIM47 maybe one of the negative regulators of autophagy among the TRIM family
499 members (Mandell et al., 2014). To test, we silenced Trim47 (siTrim47) in bEnd.3 cells in the presence or
500 absence of 2DG-mediated starvation. In gene expression study, siTrim47 induced a significant differential
501 expression of *Atg7*, *Bcl2 Gabarap*, *Gabarapl1* and *Gabarapl2* (Fig. 6A). While 2DG significantly reduced
502 expression of *Atg7* and *Gabarap* family, silencing Trim47 in bEnd.3 cells doubled this expression in all
503 conditions (Fig. 6B). *Atg7* is an essential regulator of cytoplasmic to vacuole transport in autophagy while

504 the *Gabarap* family is important for the formation of late autophagosome, and these suggested that the loss
505 of Trim47 may disinhibit autophagy, especially at the later stage. Indeed, in immunocytochemistry, gene
506 silencing of *Trim47* augmented the expression of p-p62^{Ser349}, p-ULK1^{Ser555} and GABARAP in bEnd.3 cells
507 independent of 2DG-mediated starvation (Fig. C-E). Neither siTrim47 nor 2DG altered the number of p-
508 ULK^{+} cells but siTrim47 significantly increased the number of p-ULK1$^{Ser555+}$ in each positive cell (P =
509 0.0097, Fig. 6F). While only 2DG significantly induced p-p62 expressing cells (P = 0.0028) and p-p62
510 punta per cell (P = 0.0139), siTrim47 induced the highest number of p-p62 punta per cell (vs Control, P =
511 0.0424, Fig. 6G). Silencing Trim47 also significantly increased the percentage of GABARAP-expressing
512 cells (P = 0.0009), but the number of GABARAP punta was unaffected by either treatment (Fig. 6H). The
513 examination of LC3B showed that siTrim47 significantly increased the number of LC3B^{+} bEnd.3 cells with
514 or without 2DG treatment (Fig. 6I). Importantly, the loss of Trim47 also increased the percentage of cells
515 with vacuole formation (Fig. 6J, K). Quantifications showed that siTrim47 increased LC3B^{+} b.End3 cells
516 a 2.2-fold and 2.8-fold in control and 2DG treatment, respectively (Fig. 6L). Although siTrim47 did not
517 increase the number of LC3B^{+} punta, it significantly increased the number of vacuole positive cells by 4.8
518 and 7.6 folds in control and 2DG treatment, respectively (Fig. 6M). Together, these data indicate that the
519 loss of Trim47 may disinhibit autophagy in brain ECs and suggested that Trim47 is an endogenous inhibitor
520 of autophagy.

521 Among the SNPs of *TRIM47* at 17q25 that leads WMH, only one missense variant (rs4600514;
522 NP_258411.2; p.R187W) has potentially damaging consequences (Mishra et al., 2022). It remains unknown
523 whether this mutation will lead to the loss-of-function or gain-of toxicity-effects on brain ECs. To
524 investigate, we tracked the location of R187 in the predicted 3D structure of human TRIM47 and mouse
525 Trim47 protein (equivalent to R191) (Fig. 7A, B). In both models, the location of this residue is situated in
526 the RING-finger domain which is responsible for E3 ubiquitin ligase function. However, this residue is far
527 from the LIR motif (NQWEQL or SQWEQL) that is responsible for autophagy function. Yet, TRIM family
528 members are known to form homodimer, heterodimer and oligomer which may in turn contribute to the
529 recognition of diverse substrates and catalytic regulations (Koliopoulos et al., 2016; Koliopoulos et al.,
530 2018). We asked if the TRIM47 model may form the anti-parallel coiled-coil dimerization as in TRIM25
531 (Koliopoulos et al., 2018; Sanchez et al., 2014), and whether the residue at R187 may have any implications
532 on the dimerization (Fig. 7C-E). The *in silico* simulation showed that it is likely that TRIM47 may form
533 coiled-coil dimerization as in TRIM25, but the RING-finger domain remains distant from the dimerization
534 sites (Fig. 7C - E). To validate the TRIM47 dimerization, we resolved proteins isolated from bEnd.3 cells
535 treated with 2DG in PAGE without sodium dodecyl sulfate denaturation. A significant increase of potential
536 TRIM47 dimers at approximately 140 kDa (143.4 ± 2.5 kDa) and 130 kDa (134.6 ± 2.3 kDa) were
537 identified. In such non-denaturing condition, a putative oligomer above 250 kDa was also observed (Fig.
538 7F). Given the size of Trim47 monomer is 70 kDa, these findings suggested that Trim47 may form
539 homodimer or heterodimer. In addition, the potential formation of coiled-coil dimerization is the basis of
540 the formation of a hexagon mesh network in TRIM5/TRIM5α which bridges the RING domains between
541 two molecules and provide a scaffold as an oligomer for autophagy (Carter et al. 2020; Mandell et al. 2014).
542 The dimerization and putative oligomerization of TRIM47 suggested that a similar oligomerization is
543 plausible (Fig. 7G).
544

545 **Discussion**

546 WMH formation is highly correlated with cognitive decline in aging and the progression of age-
547 related dementia. The common identification of genetic risk locus at 17q25 found in GWAS studies has
548 provided clues towards the molecular mechanism of WMH formation (Fornage et al., 2011; Persyn et al.,
549 2020; Traylor et al., 2019; Verhaaren et al., 2015). Here, we proposed that *TRIM47*, one of the two TRIM
550 family members at this genetic locus, is selectively expressed in the brain ECs and plays a role in autophagy.
551 We identified the potential binding sites with the key autophagy adaptor LC3B *in silico* and found that
552 TRIM47 is a negative regulator of autophagy *in vitro*. Autophagy is the key process for ECs remodeling

during hypertension flux (Vion et al., 2017), and, in turn, hypertension is a major physiological risk factor for WMH formation (Chesebro et al., 2020; Hajjar et al., 2011; Verhaaren et al., 2013). Our results support that dysfunctional TRIM47 disrupts brain ECs autophagy which might lead to WMH formation.

The 80 plus members of the TRIM family not only serve as E3 ubiquitin ligases, but also plays a role in autophagy. In a systemic knockdown screening of 67 human *TRIM* in HeLa cells, it was found that TRIM members can be positive (TRIM3, -5, -6, -22, -23, -28, -31, -34, -38, -41, -42, -44, -45, -48 to -50, -55, -58, -59, -61, -73, and -74) or negative (TRIM1, -2, -10, -17, -26, -33, -51, -65, -72, and -76) regulators of autophagy at different stages (Di Rienzo et al., 2020; Mandell et al., 2014). Our hypothesis that TRIM47 dysfunction may lead to EC pathology during WMH formation is supported by a recent study showing that the knockdown of TRIM47 resulted in an increase of EC permeability *in vitro* (Mishra et al., 2022). Nevertheless, this study did not address the cellular mechanism connecting the TRIM47 loss-of-function and permeability change. The two key cellular homeostasis processes important for EC functions, ubiquitination and autophagy (Majolee et al., 2019; Meng et al., 2022), are both regulated by TRIMs. TRIM47 was showed to regulate TNFα-mediated lung EC activation by degrading TRAF2 through K63 ubiquitination (Qian et al., 2022), but its role in autophagy is unknown. Here, we confirmed that TRIM47 is selectively expressed in the ECs of human and mouse brain, and we demonstrated that *TRIM47* is downregulated among the relevant models of hypertension in EC with ongoing autophagy. Of note, we observed that *Trim47* transcription shifts occur acutely (days) upon experimental ischemic models (see Table S3) and returns to normal in chronic models (weeks). Indeed, in our recent report, we detected minimal *Trim47* transcription change in the mouse corpus callosum after a four-weeks bilateral carotid artery stenosis model simulating subcortical ischemic vascular dementia (Takase et al., 2021). These observations suggest that TRIM47 may regulate autophagy at the early stage of cerebral ischemia. TRIM family members regulate autophagy at different stages by targeting adaptor proteins such as AMPK, ULK1 or Beclin1, it is also proposed that these proteins form a TRIM-containing complex during autophagosome formation (Di Rienzo et al., 2020). As in TRIM5α, a positive regulator of autophagy (Mandell et al., 2014), we identified the LIR motif (NEWEQL) in TRIM47 and its potential binding partner residues in LC3B using *in silico* and such interaction was visualized by the super resolution microscopy.

The putative interaction with LC3B may confer the autophagy regulatory function to TRIM47. In bEnd.3 cells, autophagy inhibition mediated by 3-MA and autophagy activation mediated by rapamycin were associated with Trim47 upregulation and downregulation, respectively. This opposing expression pattern suggested that Trim47 may regulate autophagy in EC. The gene silencing experiment confirmed that Trim47 is a negative regulator of autophagy in brain ECs. Other TRIM family members negatively regulate autophagy by targeting different key autophagic factors such as TFEB (Wang et al., 2018), AMPK (Pineda et al., 2015) or Beclin1 (Han et al., 2018) through proteasome degradation, transcription or microRNA regulations (Di Rienzo et al., 2020). These regulatory functions of TRIM protein are highly associated with their intracellular distribution, for instance, TRIM52 regulate immune functions by acting in the nucleus (Fan et al., 2017) while TRIM20 regulates E3 ligase functions in the cytoplasm (Hatakeyama, 2017). The dual localization of Trim47 suggested that it may serve autophagy regulatory functions in the nucleus and cytoplasm of brain ECs. Silencing Trim47 not only resulted in a significant upregulation of players (*Atg7 Bcl2* and *Gabarap*) important for in autophagosome formation (Collier et al., 2021; Ma et al., 2013), but also increased the ECs with phosphorylation of ULK1 and p62 as well as vacuole formation. As ULK-mediates the phosphorylation of p62 (Ikeda et al., 2023), Trim47 is therefore pivotal to both early and later stage of autophagy (Egan et al., 2015). TRIM65, the other TRIM member at locus 17q25, is known to inhibit autophagy also by controlling *Atg7* expression in lung cancer cells (Pan et al., 2019). It remains obscure whether the TRIM47 and TRIM65 mediate autophagy regulation by jointly targeting *Atg7* in brain ECs, but it warrants further investigation.

As shown in the TRIM47 *in silico* model, the possible pathogenic missense variant (rs600514, missense, NP_258411.2: p.Arg187Trp) is located in the RING domain and may have a direct implication

603 on the E3 ligase activity. Yet, TRIM members are known to form homodimer, heterodimer and oligomer
604 in order to function (Hatakeyama, 2017) (Fig. 7G). First, the self-association of two TRIM monomers is
605 enabled by the highly conserved coiled coil which form an interdigitating anti-parallel helical hairpin
606 (Sanchez et al., 2014), and such homodimer is proposed to be the building block of the oligomers in
607 TRIM5/TRIM5α. Second, the dimerization between the RING domain is critical for E3 ligase activity and
608 is conserved among TRIM subfamily C-IV (including TRIM5/TRIM5α, TRIM21, TRIM25 and TRIM69)
609 where TRIM47 belongs (Fiorentini et al., 2020). Finally, as exemplified by TRIM5/TRIM5α, these coiled-
610 coil homodimers with the RING domain at both ends may form a hexagon mesh of network that may be
611 part of the scaffold (TRIMosome) to facilitate autophagy (Carter et al., 2020; Mandell et al., 2014). Here,
612 we showed that TRIM47 may dimerize, and such dimer increased in pro-autophagy condition. Although
613 the distance (194 amino acids) between the RING domains and LIR motif at the PRY domain appears to
614 make the missense variant more relevant to ubiquitination than to autophagy, the dimerization or
615 oligomerization of TRIM47 may impact on both E3 ligase activity and autophagy. As a speculation, the
616 TRIM family forms heterodimer with structurally related members (Sanchez et al., 2014). As TRIM47 and
617 TRIM65 belong to the same subfamily C-IV (Hatakeyama, 2017), it remains an open question whether both
618 of the protein variants encoded at 17q25 may form a pathogenic heterodimer leading to WMH formation.
619
620 To conclude, one of the genetic risk factors of WMH formation, TRIM47, is selectively expressed
621 in brain ECs and is a negative regulator of autophagy. Cerebrovasculature is a highly dynamic system,
622 where the flexibility is conferred by the autophagy process of the ECs (Kim et al., 2018). Our findings
623 support that dysfunctional TRIM47 may contribute to autophagy failure in brain EC and therefore confer
624 the risk of WMH development by harnessing the remodeling of cerebrovasculature, especially in
625 hypertension (de Montgolfier et al., 2019).
626
627
628
629
630
631
632
633
634
635
636
637
638
639
640
641
642
643
644

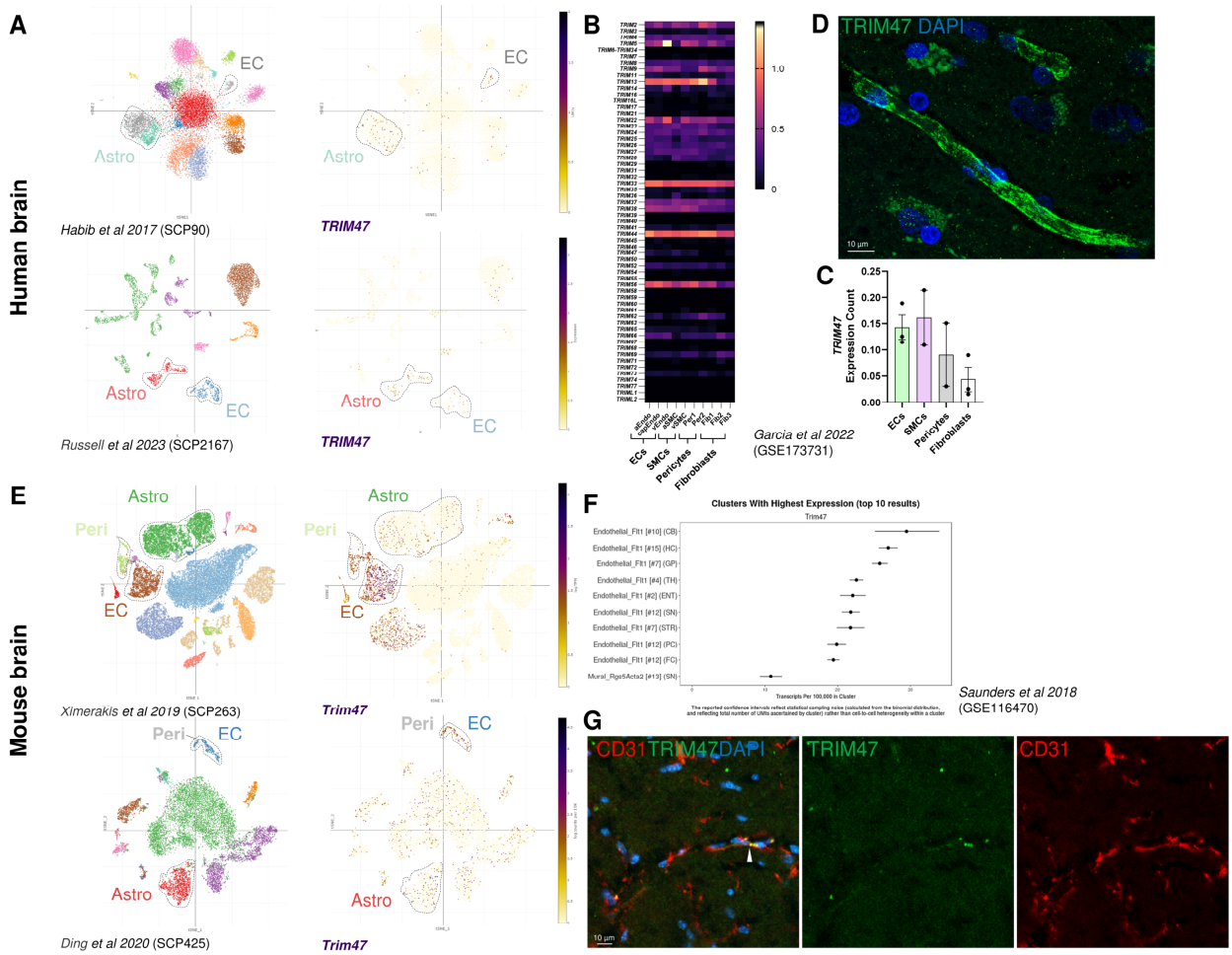

Figure 1. *TRIM47* expression is enriched in brain ECs in human and mouse

A Single cell portal-based scRNAseq exploration with t-SNE (t-distributed stochastic neighbour embedding) visualization of gene expression in human brain tissue (accession: SCP90, SCP2167). *Left*, t-SNE representation of all detect brain cell types *Right*, t-SNE representation of human *TRIM47* expression enriched in the brain endothelial cells and astrocytes. All cell labels are colour coded to the tSNE map. **B** Exploration of *TRIM* family transcription in a scRNAseq library of healthy human cerebrovascular cells (GSE173731), with *TRIM47* expression shown on **C**. **D** Representative *TRIM47* (green) immunohistochemistry image of the healthy human frontal cortex confirming the specific expression on endothelial cells. **E** Single cell portal-based scRNAseq exploration with t-SNE visualization of gene expression in mouse (wildtype) brain tissues (accession: SCP263, SCP425). *Left*, t-SNE representation of all detected brain cell types *Right*, t-SNE representation of mouse *Trim47*expression enriched in the Fit1^{+} endothelial cells. **F** Exploration of in a third scRNAseq of a mouse (wildtype) brain across nine regions showing brain ECs has the highest *Trim47* expression in all regions. **G** Representative immunohistochemistry image of the wildtype mouse corpus callosum confirming the specific Trim47 expression (green) on CD31^{+} endothelial cells (red). aEndo, arterioles endothelial cells; capEndo, capillary endothelial cells; vEndo, venule endothelial cells; aSMC, arterioles smooth muscle cell; vSMC, venule smooth muscle cell; Per1/Per2, Pericytes; Fib1/Fib2/Fib3, fibroblasts. FC, frontal cortex; PC, posterior cortex; SN, substantia nigra; STR, striatum; TH, thalamus; GP, globus pallidus; ENT, entopeduncular; HC, hippocampus and CB, cerebellum.

653

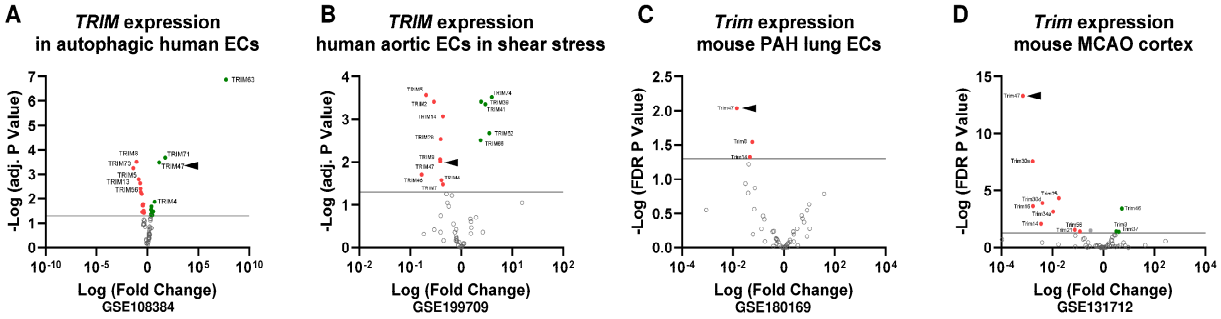

654

Figure 2. TRIM family transcription across hypertensive and cardiovascular disorder models in human and mouse

A *TRIM47* expression was significantly regulated in primary HUVEC cells upon overexpression of master autophagy transcription factor TFEB **B** *TRIM47* expression was downregulated in primary human aortic ECs upon laminar shear stress stimulation, but the level return to normal after 24 hour of recovery **C** A significant downregulation of *Trim47* expression was found in mouse lung endothelial cells after 3 weeks of pulmonary arterial hypertension modelling **D** A significant downregulation of *Trim47* expression was found in mouse middle cerebral artery occlusion modelling 24 hours upon injury, but the level return to normal after 28 days of recovery. Extended data are presented see Table S2 and Table S3.

655
656
657
658
659
660
661
662
663
664
665
666
667
668
669

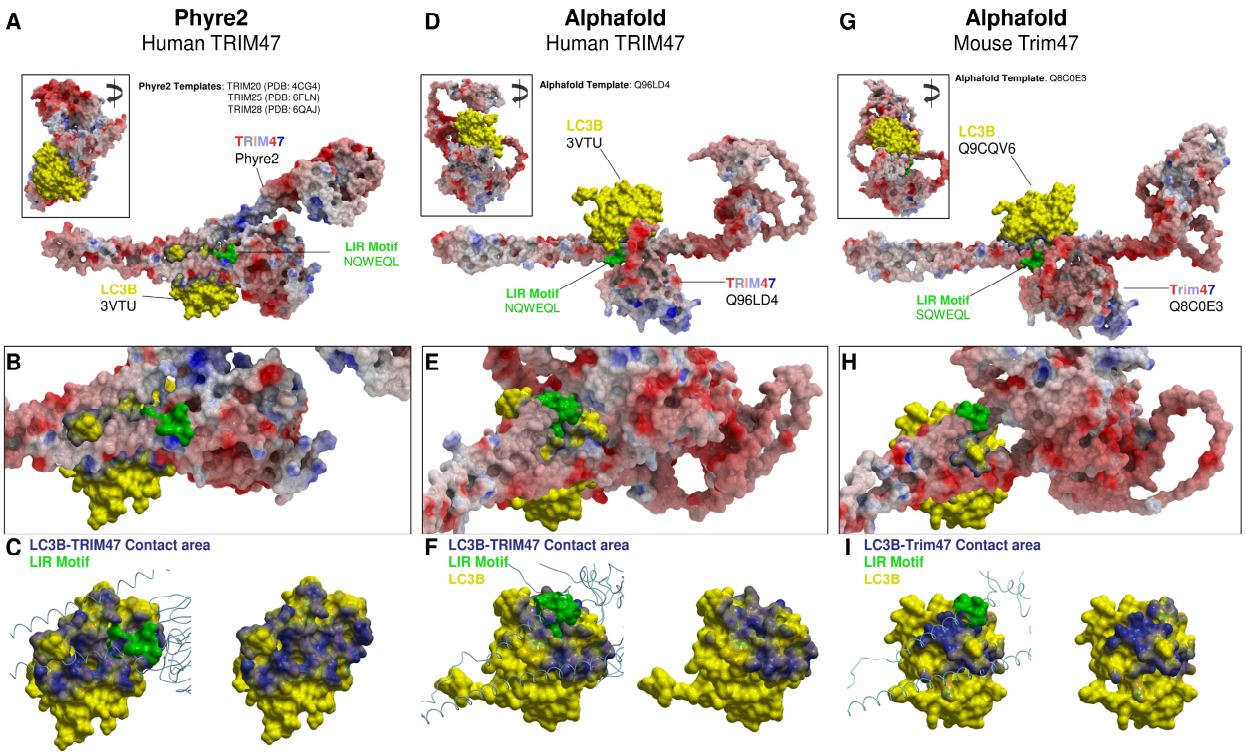

Figure 3. Simulation of xLIR motif-LCB interactions in TRIM47 *in silico*
A Phyre2 generated 3D model of TRIM47 (Red-grey-blue on electrostatic charge cartoon mesh; model based on PDB: 4CG4, 6FLN and 6QAJ) docked with human LC3B (Yellow; PDB: 3VTU) using ClusPro server (Kozakov et al., 2017).The xLIR sequence NQWEQL highlighted in green. Right 90º rotation in inset **B** Magnified view of the interaction site between xLIR and LC3B. **C** xLIR-LC3B interactions with (*left*) or without (*right*) the ribbon of xLIR (green), where the xLIR-LC3B contact area highlighted in blue. **D** Human TRIM47 generated by artificial intelligence (Red-grey-blue on electrostatic charge cartoon mesh; Alphafold: Q96LD4) docked with human LC3B (Yellow; PDB: 3VTU). The xLIR sequence NQWEQL is highlighted in green. Right 90º rotation in inset **E** Magnified view of the interaction site between xLIR and LC3B. **F** xLIR-LC3B interactions with (*left*) or without (*right*) the ribbon of xLIR (green), where the xLIR-LC3B contact area is highlighted in blue. **G** Alphafold-based Mouse Trim47 (Red-grey-blue on electrostatic charge cartoon mesh; Alphafold: Q9CQV6) docked with mouse LC3B (Yellow; Alphafold: Q8C0E3). The xLIR sequence SQWEQL highlighted in green. Right 90º rotation in inset **H** Magnified view of the interaction site between xLIR and LC3B. **I** xLIR-LC3B interactions with (*left*) or without (*right*) the ribbon of xLIR (green), where the xLIR-LC3B contact area is highlighted in blue.

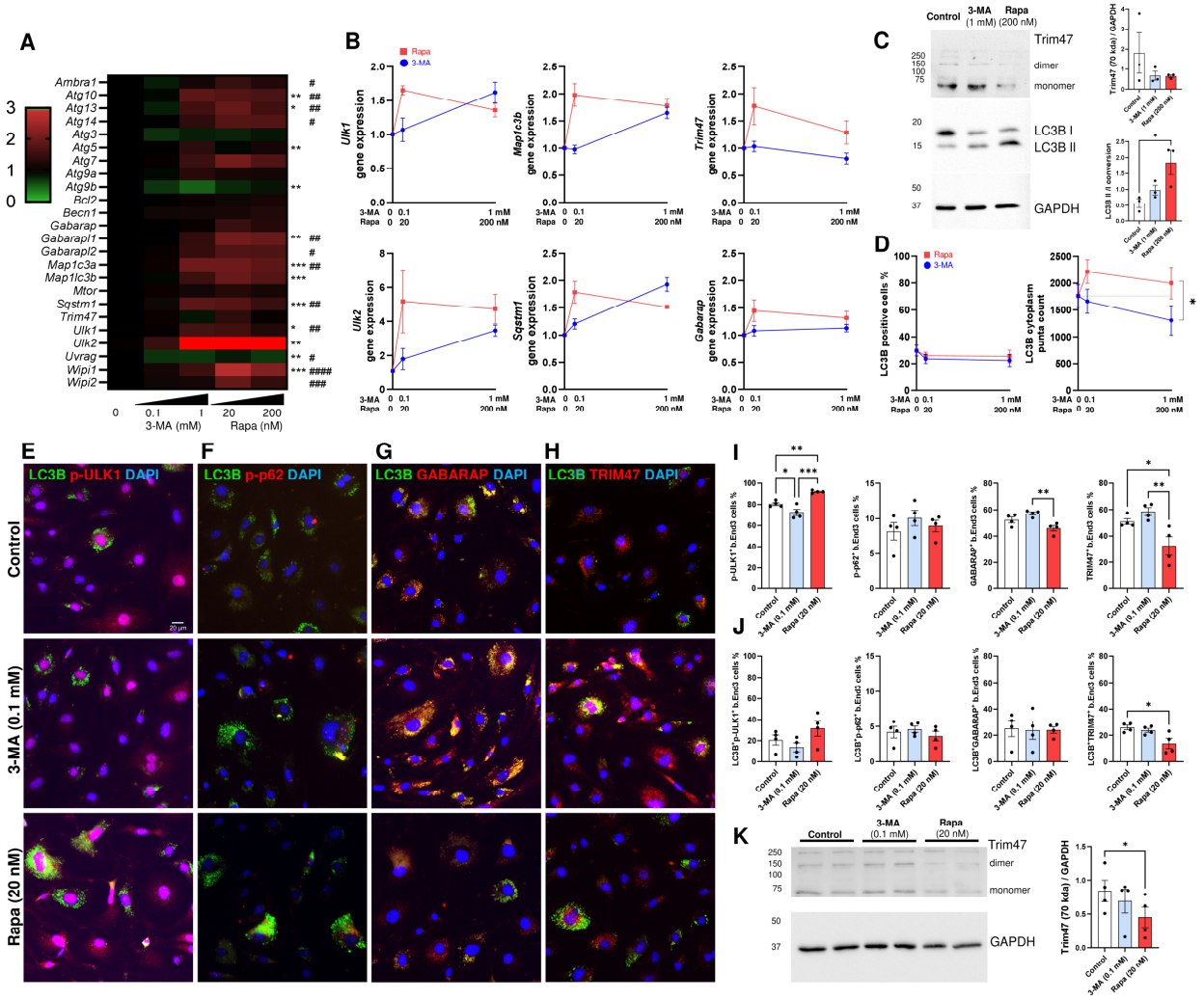

Figure 4. Trim47 expression is modulated by rapamycin-mediated autophagy induction in brain endothelial cells

A Heatmap of gene expression across autophagy related genes in bEnd.3 cells upon autophagy inhibition by 3-MA (0.1, 1 mM) and induction by Rapa (20, 200 nM). The statistical significance of gene expression changes mediated by 3-MA and Rapa were denoted by * and #, respectively. **B** The concentration dependent effects of 3-MA and Rapa were exemplified by *Ulk1*, *Ulk2*, *Map1c3b*, *Sqstm1/p62*, *Trim47* and *Gabarap* induced by 3-MA and Rapa. Of note, the high concentration of 3-MA mediated autophagy in the full medium as reported earlier (Wu et al., 2010). **C** Immunoblot showing Trim47 expression at both the monomer (70 kDa) and dimer (~140 kDa) form were reduced by autophagy induction at high concentration of 3-MA (1 mM) and Rapa (200 nM) indicated by the significant LC3B conversion. **D-G** Representative immunocytochemistry image showing the colocalization between LC3B with p-ULK1^{Ser555}, p-p62^{Ser349} GABARAP and Trim47, respectively. **H** Quantification of the LC3B^{+} cells and LC3B^{+} punta in bEnd.3 cells showed a significant difference between 3-MA and Rapa treatment. **I** Quantification of p-ULK1^{Ser555}, p-p62^{Ser349} GABARAP and Trim47-expressing cells upon 3-MA and Rapa treatment. **J** Quantification of colocalization between LC3B with p-ULK1^{Ser555}, p-p62^{Ser349} GABARAP or Trim47 showed a significant reduction of Trim47-LC3B double positive cells upon Rapa treatment. **K** Immunoblot showing the reduction of Trim47 monomer (70 kDa) by low concentration of Rapa (20 nM), but not 3-MA (0.1 mM), as in the immunocytochemistry. One-way ANOVA repeated measures followed by Tukey's multiple comparisons test (* or #, $p < 0.05$; ** or ## $P<0.01$, *** or ###, $P<0.001$, ####, $P<0.0001$).

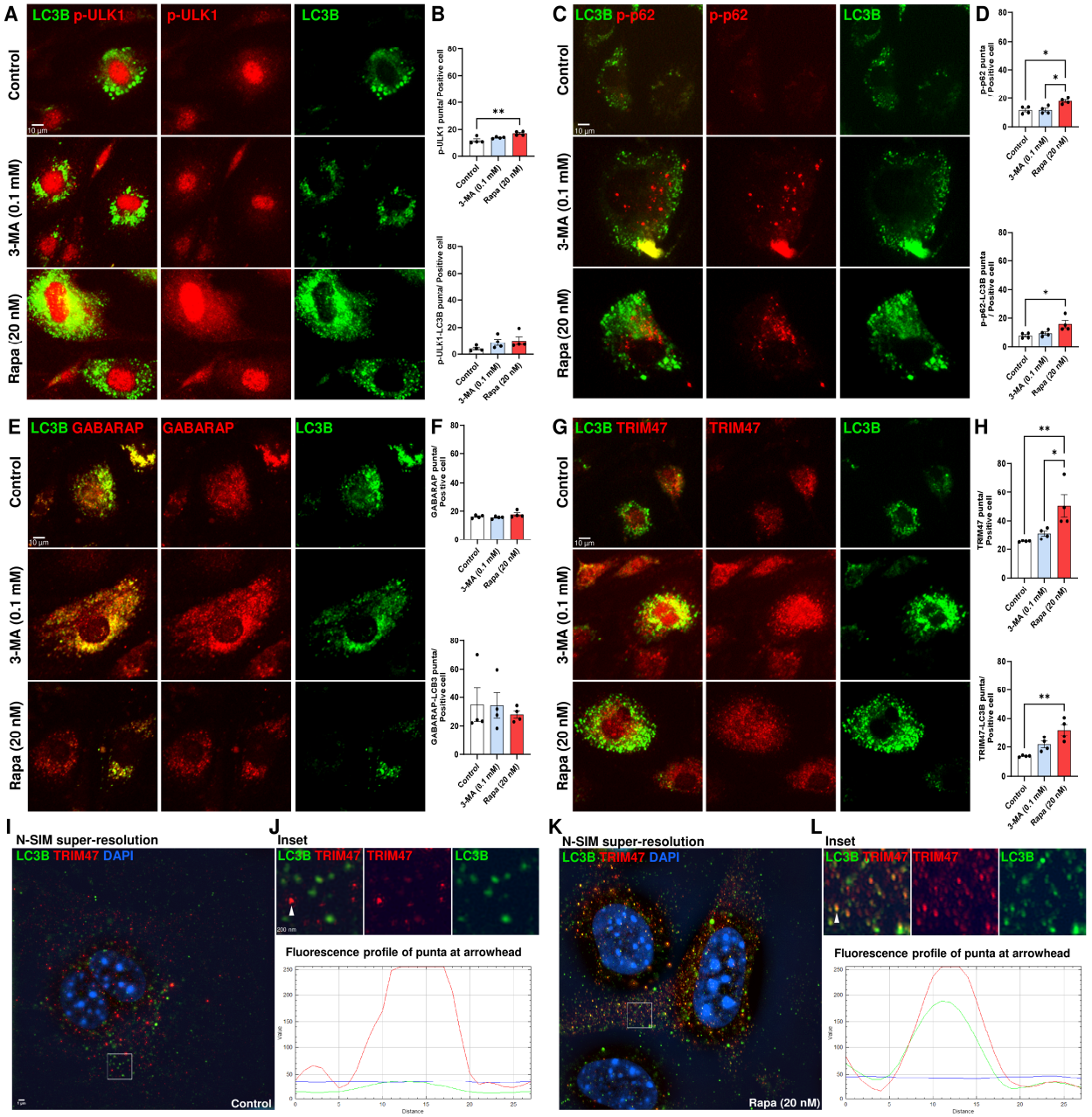

Figure 5. Trim47 colocalization with LC3B in autophagic brain endothelial cells
Representative immunocytochemistry image and quantification of **A, B** LC3B-p-ULK1^{Ser555}, **C, D** LC3B-p-p62 (p-p62^{Ser349}), **E, F** LC3B-GABARAP, and **G, H** LC3B-Trim47 colocalization in control, 3-MA, or Rapa treatment. **I** Structured Illumination Microscopy (SIM)-based super-resolution image of the LC3B and Trim47 at close proximity under control condition, which the inset area shown at a higher magnification in **J**. The colour profile plot below demonstrates the lack of Trim47-LC3 colocalization in control. **K** SIM-based super-resolution image of the LC3B and Trim47 at close proximity after Rapa treatment (20 nM, 24 h), in which the inset area is magnified in **L**. The colour profile plot below confirmed the colocalization of Trim47-LC3 punta during autophagy. One-way ANOVA repeated measures followed by Tukey's multiple comparisons test (*p < 0.05; ** P<0.01). **I, J** and **K, L** share the same scale with scale bar = 1 µm and 200 nm, respectively.

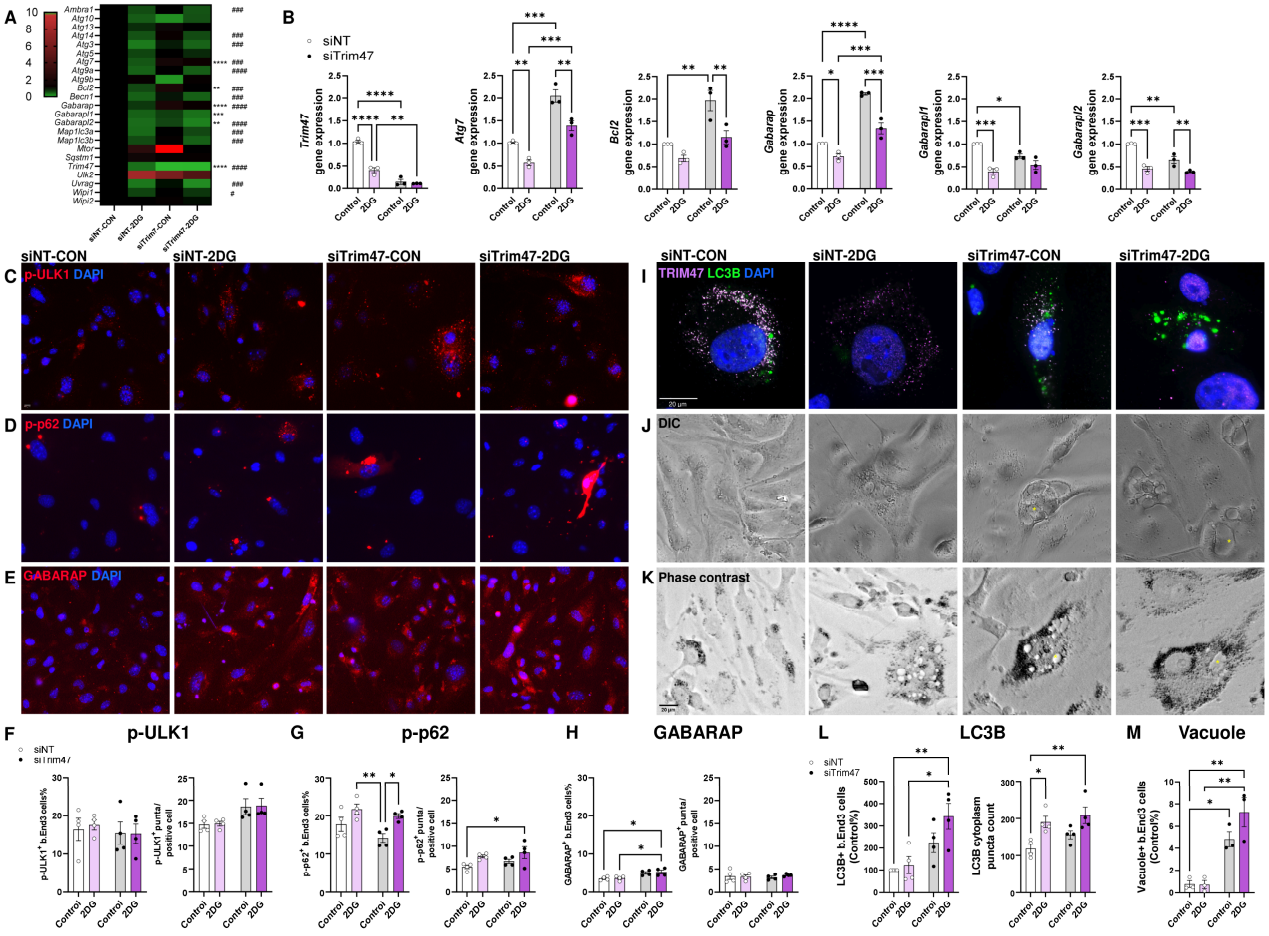

Figure 6. Silencing Trim47 increased autophagy in brain endothelial cells

A Heatamp of gene expression analysis of b.End3 cells with non-targeted gene silencing (siNT) and siTrim47 with or without 2DG-mediated starvation Two-way ANOVA repeated measures followed by Holm-Šídák's multiple comparisons test (*p < 0.05, ** P<0.01, ***P<0.001, ****P<0.0001). **B** Individual gene expression analysis of *Trim47, Atg7, Bcl2, Gabarap, Gabarapl1* and *Gabarapl2* demonstrating that the loss of *Trim47* disinhibit autophagy. **C-E** Representative immunocytochemistry image of bEnd.3 cells expressing p-ULK1^{Ser555}, p-p62^{Ser349} and GABARAP treated by siNT or siTrim47 with or without 2DG treatment. **F-H** Quantifications of p-ULK1^{Ser555}, p-p62^{Ser349} and GABARAP expressing upon siTrim47 with or without 2DG starvation were shown, where **F** silencing Trim47 significantly increased the number of p-ULK1$^{Ser555+}$ punta in each positive cell (P = 0.0097), **G** induced the highest number of p-p62 punta per cell (vs Control, P = 0.0424) and **H** significantly increased the percentage of GABARAP-expressing cells (P = 0.0009). **I** Representative immunocytochemistry image showing the effect of siTrim47 and 2DG on LC3B and Trim47 expression in b.End3 cells. **J, K** Differential interference contrast (DIC) and phase contrast of bEnd.3 cells showing vacuole formation (*) under siTrim47 conditions, respectively. **L, M** Quantification of LC3B^{+} cells, LC3B^{+} punta per cell, and vacuole formation showing that sip-pTrim47 significantly increases autophagy responses in bEnd.3 cells. Two-way ANOVA followed by Tukey multiple comparisons test (*p < 0.05, ** P<0.01).

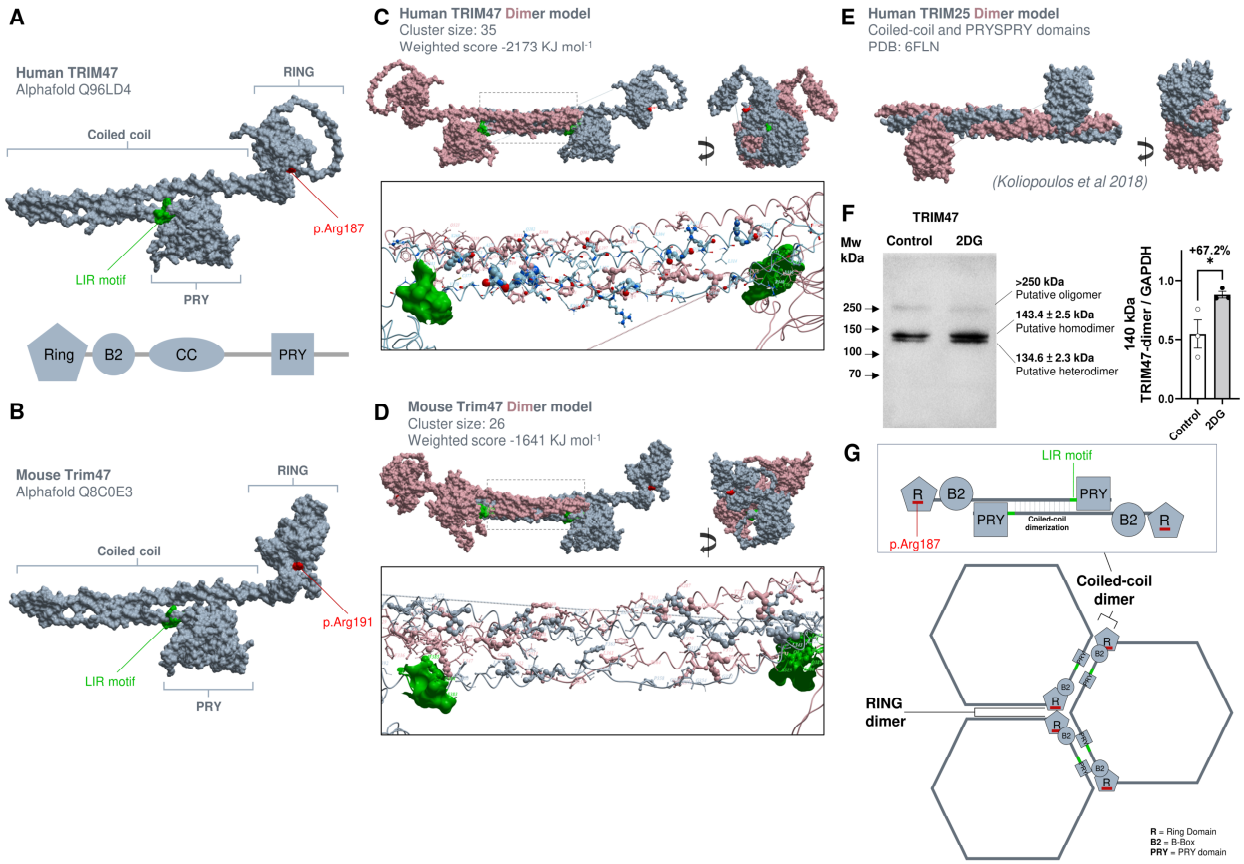

692

Figure 7. WMH associated SNP is located at the RING region of TRIM47 at distance from LIR motif
The *in silico* model demonstrating **A** human TRIM47 protein and **B** mouse Trim47 structure with the location of the LIR motif in green and the missense variant p.Arg187 (p.Arg191 in mouse) shown in red. **C, D** ClusPro-based simulation of coiled-coil homodimer of human and mouse TRIM47 model demonstrating the distance between two LIR motif (green) and the lack of interactions between the missense variant p.Arg187 (red) in the RING domain. **E** Reproduced TRIM25 coiled-coil homodimer model described by Koliopoulos et al 2018. F Immunoblotting of bEnd.3 lysate in control and 2DG-treatment resolved under non-denaturing conditions showing the increase of Trim47 dimers at ~140 kDa (143.4 ± 2.5 kDa) and 130 kDa (134.6 ± 2.3 kDa), respectively. The 140 kDa dimer is likely a homodimer of Trim47 (monomer = 70 kDa), while the 130 kDa dimer could be a heterodimer with other Trim family members. An additional band at above 250 kDa suggested that the Trim47 might form oligomers. **G** The formation of TRIM47 coiled-coil homodimers could be the basic building block that may allow the formation of an oligomer as a hexagon mesh of network that may be part of the scaffold (TRIMosome) to facilitate autophagy as earlier described in TRIM5/TRIM5α (Carter et al. 2020; Mandell et al. 2014).

693
694
695
696
697
698
699
700

701 **Reference**

702 Abagyan, R., M. Totrov, and D. Kuznetsov. 1994. ICM—A new method for protein modeling and design:
703 Applications to docking and structure prediction from the distorted native conformation. *Journal*
704 *of Computational Chemistry*. 15:488-506.
705 Alber, J., S. Alladi, H.J. Bae, D.A. Barton, L.A. Beckett, J.M. Bell, S.E. Berman, G.J. Biessels, S.E.
706 Black, I. Bos, G.L. Bowman, E. Brai, A.M. Brickman, B.L. Callahan, R.A. Corriveau, S. Fossati,
707 R.F. Gottesman, D.R. Gustafson, V. Hachinski, K.M. Hayden, A.M. Helman, T.M. Hughes, J.D.
708 Isaacs, A.L. Jefferson, S.C. Johnson, A. Kapasi, S. Kern, J.C. Kwon, J. Kukolja, A. Lee, S.N.
709 Lockhart, A. Murray, K.E. Osborn, M.C. Power, B.R. Price, H.F.M. Rhodius-Meester, J.A.
710 Rondeau, A.C. Rosen, D.L. Rosene, J.A. Schneider, H. Scholtzova, C.E. Shaaban, N. Silva, H.M.
711 Snyder, W. Swardfager, A.M. Troen, S.J. van Veluw, P. Vemuri, A. Wallin, C. Wellington, D.M.
712 Wilcock, S.X. Xie, and A.H. Hainsworth. 2019. White matter hyperintensities in vascular
713 contributions to cognitive impairment and dementia (VCID): Knowledge gaps and opportunities.
714 *Alzheimers Dement (N Y)*. 5:107-117.
715 Au, R., J.M. Massaro, P.A. Wolf, M.E. Young, A. Beiser, S. Seshadri, R.B. D'Agostino, and C. DeCarli.
716 2006. Association of white matter hyperintensity volume with decreased cognitive functioning:
717 the Framingham Heart Study. *Arch Neurol*. 63:246-250.
718 Bankhead, P., M.B. Loughrey, J.A. Fernandez, Y. Dombrowski, D.G. McArt, P.D. Dunne, S. McQuaid,
719 R.T. Gray, L.J. Murray, H.G. Coleman, J.A. James, M. Salto-Tellez, and P.W. Hamilton. 2017.
720 QuPath: Open source software for digital pathology image analysis. *Sci Rep*. 7:16878.
721 Barrett, T., S.E. Wilhite, P. Ledoux, C. Evangelista, I.F. Kim, M. Tomashevsky, K.A. Marshall, K.H.
722 Phillippy, P.M. Sherman, M. Holko, A. Yefanov, H. Lee, N. Zhang, C.L. Robertson, N. Serova,
723 S. Davis, and A. Soboleva. 2013. NCBI GEO: archive for functional genomics data sets--update.
724 *Nucleic Acids Res*. 41:D991-995.
725 Bridges, L.R., J. Andoh, A.J. Lawrence, C.H.L. Khoong, W. Poon, M.M. Esiri, H.S. Markus, and A.H.
726 Hainsworth. 2014. Blood-brain barrier dysfunction and cerebral small vessel disease
727 (arteriolosclerosis) in brains of older people. *J Neuropathol Exp Neurol*. 73:1026-1033.
728 Brown, R., A. Low, and H.S. Markus. 2021. Rate of, and risk factors for, white matter hyperintensity
729 growth: a systematic review and meta-analysis with implications for clinical trial design. *J Neurol*
730 *Neurosurg Psychiatry*. 92:1271-1277.
731 Carter, S.D., J.I. Mamede, T.J. Hope, and G.J. Jensen. 2020. Correlated cryogenic fluorescence
732 microscopy and electron cryo-tomography shows that exogenous TRIM5alpha can form
733 hexagonal lattices or autophagy aggregates in vivo. *Proc Natl Acad Sci U S A*. 117:29702-29711.
734 Cheng, A., K.H. Tse, H.M. Chow, Y. Gan, X. Song, F. Ma, Y.X.Y. Qian, W. She, and K. Herrup. 2020.
735 ATM loss disrupts the autophagy-lysosomal pathway. *Autophagy*:1-13.
736 Chesebro, A.G., J.D. Melgarejo, R. Leendertz, K.C. Igwe, P.J. Lao, K.K. Laing, B. Rizvi, M. Budge, I.B.
737 Meier, G. Calmon, J.H. Lee, G.E. Maestre, and A.M. Brickman. 2020. White matter
738 hyperintensities mediate the association of nocturnal blood pressure with cognition. *Neurology*.
739 94:e1803-e1810.
740 Collier, J.J., F. Suomi, M. Olahova, T.G. McWilliams, and R.W. Taylor. 2021. Emerging roles of ATG7
741 in human health and disease. *EMBO Mol Med*. 13:e14824.
742 De Meyer, G.R., M.O. Grootaert, C.F. Michiels, A. Kurdi, D.M. Schrijvers, and W. Martinet. 2015.
743 Autophagy in vascular disease. *Circ Res*. 116:468-479.
744 de Montgolfier, O., A. Pincon, P. Pouliot, M.A. Gillis, J. Bishop, J.G. Sled, L. Villeneuve, G. Ferland,
745 B.I. Levy, F. Lesage, N. Thorin-Trescases, and E. Thorin. 2019. High Systolic Blood Pressure
746 Induces Cerebral Microvascular Endothelial Dysfunction, Neurovascular Unit Damage, and
747 Cognitive Decline in Mice. *Hypertension*. 73:217-228.
748 Di Rienzo, M., A. Romagnoli, M. Antonioli, M. Piacentini, and G.M. Fimia. 2020. TRIM proteins in
749 autophagy: selective sensors in cell damage and innate immune responses. *Cell Death Differ*.
750 27:887-902.

751 Ding, J., X. Adiconis, S.K. Simmons, M.S. Kowalczyk, C.C. Hession, N.D. Marjanovic, T.K. Hughes,
752 M.H. Wadsworth, T. Burks, L.T. Nguyen, J.Y.H. Kwon, B. Barak, W. Ge, A.J. Kedaigle, S.
753 Carroll, S. Li, N. Hacohen, O. Rozenblatt-Rosen, A.K. Shalek, A.C. Villani, A. Regev, and J.Z.
754 Levin. 2020. Systematic comparison of single-cell and single-nucleus RNA-sequencing methods.
755 *Nat Biotechnol*. 38:737-746.
756 Egan, D.F., M.G. Chun, M. Vamos, H. Zou, J. Rong, C.J. Miller, H.J. Lou, D. Raveendra-Panickar, C.C.
757 Yang, D.J. Sheffler, P. Teriete, J.M. Asara, B.E. Turk, N.D. Cosford, and R.J. Shaw. 2015. Small
758 Molecule Inhibition of the Autophagy Kinase ULK1 and Identification of ULK1 Substrates. *Mol*
759 *Cell*. 59:285-297.
760 Fan, W., T. Liu, X. Li, Y. Zhou, M. Wu, X. Cui, H. Chen, and P. Qian. 2017. TRIM52: A nuclear TRIM
761 protein that positively regulates the nuclear factor-kappa B signaling pathway. *Mol Immunol*.
762 82:114-122.
763 Fan, Y., H. Lu, W. Liang, M.T. Garcia-Barrio, Y. Guo, J. Zhang, T. Zhu, Y. Hao, J. Zhang, and Y.E.
764 Chen. 2018. Endothelial TFEB (Transcription Factor EB) Positively Regulates Postischemic
765 Angiogenesis. *Circ Res*. 122:945-957.
766 Fazekas, F., R. Kleinert, H. Offenbacher, R. Schmidt, G. Kleinert, F. Payer, H. Radner, and H. Lechner.
767 1993. Pathologic correlates of incidental MRI white matter signal hyperintensities. *Neurology*.
768 43:1683-1689.
769 Fiorentini, F., D. Esposito, and K. Rittinger. 2020. Does it take two to tango? RING domain self-
770 association and activity in TRIM E3 ubiquitin ligases. *Biochem Soc Trans*. 48:2615-2624.
771 Fornage, M., S. Debette, J.C. Bis, H. Schmidt, M.A. Ikram, C. Dufouil, S. Sigurdsson, T. Lumley, A.L.
772 DeStefano, F. Fazekas, H.A. Vrooman, D.K. Shibata, P. Maillard, A. Zijdenbos, A.V. Smith, H.
773 Gudnason, R. de Boer, M. Cushman, B. Mazoyer, G. Heiss, M.W. Vernooij, C. Enzinger, N.L.
774 Glazer, A. Beiser, D.S. Knopman, M. Cavalieri, W.J. Niessen, T.B. Harris, K. Petrovic, O.L.
775 Lopez, R. Au, J.C. Lambert, A. Hofman, R.F. Gottesman, M. Garcia, S.R. Heckbert, L.D.
776 Atwood, D.J. Catellier, A.G. Uitterlinden, Q. Yang, N.L. Smith, T. Aspelund, J.R. Romero, K.
777 Rice, K.D. Taylor, M.A. Nalls, J.I. Rotter, R. Sharrett, C.M. van Duijn, P. Amouyel, P.A. Wolf,
778 V. Gudnason, A. van der Lugt, E. Boerwinkle, B.M. Psaty, S. Seshadri, C. Tzourio, M.M.
779 Breteler, T.H. Mosley, R. Schmidt, W.T. Longstreth, C. DeCarli, and L.J. Launer. 2011. Genome-
780 wide association studies of cerebral white matter lesion burden: the CHARGE consortium. *Ann*
781 *Neurol*. 69:928-939.
782 Forte, M., F. Bianchi, M. Cotugno, S. Marchitti, E. De Falco, S. Raffa, R. Stanzione, F. Di Nonno, I.
783 Chimenti, S. Palmerio, F. Pagano, V. Petrozza, A. Micaloni, M. Madonna, M. Relucenti, M.R.
784 Torrisi, G. Frati, M. Volpe, S. Rubattu, and S. Sciarretta. 2020. Pharmacological restoration of
785 autophagy reduces hypertension-related stroke occurrence. *Autophagy*. 16:1468-1481.
786 Garcia, F.J., N. Sun, H. Lee, B. Godlewski, H. Mathys, K. Galani, B. Zhou, X. Jiang, A.P. Ng, J.
787 Mantero, L.H. Tsai, D.A. Bennett, M. Sahin, M. Kellis, and M. Heiman. 2022. Single-cell
788 dissection of the human brain vasculature. *Nature*. 603:893-899.
789 Gouw, A.A., A. Seewann, H. Vrenken, W.M. van der Flier, J.M. Rozemuller, F. Barkhof, P. Scheltens,
790 and J.J. Geurts. 2008. Heterogeneity of white matter hyperintensities in Alzheimer's disease: post-
791 mortem quantitative MRI and neuropathology. *Brain*. 131:3286-3298.
792 Grunwald, D.S., N.M. Otto, J.M. Park, D. Song, and D.H. Kim. 2020. GABARAPs and LC3s have
793 opposite roles in regulating ULK1 for autophagy induction. *Autophagy*. 16:600-614.
794 Habes, M., G. Erus, J.B. Toledo, T. Zhang, N. Bryan, L.J. Launer, Y. Rosseel, D. Janowitz, J. Doshi, S.
795 Van der Auwera, B. von Sarnowski, K. Hegenscheid, N. Hosten, G. Homuth, H. Volzke, U.
796 Schminke, W. Hoffmann, H.J. Grabe, and C. Davatzikos. 2016. White matter hyperintensities and
797 imaging patterns of brain ageing in the general population. *Brain*. 139:1164-1179.
798 Habib, N., I. Avraham-Davidi, A. Basu, T. Burks, K. Shekhar, M. Hofree, S.R. Choudhury, F. Aguet, E.
799 Gelfand, K. Ardlie, D.A. Weitz, O. Rozenblatt-Rosen, F. Zhang, and A. Regev. 2017. Massively
800 parallel single-nucleus RNA-seq with DroNc-seq. *Nat Methods*. 14:955-958.

801 Hainsworth, A.H., T. Minett, J. Andoh, G. Forster, I. Bhide, T.R. Barrick, K. Elderfield, J. Jeevahan, H.S.
802 Markus, and L.R. Bridges. 2017. Neuropathology of White Matter Lesions, Blood-Brain Barrier
803 Dysfunction, and Dementia. *Stroke*. 48:2799-2804.
804 Hajjar, I., L. Quach, F. Yang, P.H. Chaves, A.B. Newman, K. Mukamal, W. Longstreth, Jr., M. Inzitari,
805 and L.A. Lipsitz. 2011. Hypertension, white matter hyperintensities, and concurrent impairments
806 in mobility, cognition, and mood: the Cardiovascular Health Study. *Circulation*. 123:858-865.
807 Han, T., M. Guo, M. Gan, B. Yu, X. Tian, and J.B. Wang. 2018. TRIM59 regulates autophagy through
808 modulating both the transcription and the ubiquitination of BECN1. *Autophagy*. 14:2035-2048.
809 Hasan-Olive, M.M., H.A. Hansson, R. Enger, E.A. Nagelhus, and P.K. Eide. 2019. Blood-Brain Barrier
810 Dysfunction in Idiopathic Intracranial Hypertension. *J Neuropathol Exp Neurol*. 78:808-818.
811 Hatakeyama, S. 2017. TRIM Family Proteins: Roles in Autophagy, Immunity, and Carcinogenesis.
812 *Trends Biochem Sci*. 42:297-311.
813 Ichimura, Y., S. Waguri, Y.S. Sou, S. Kageyama, J. Hasegawa, R. Ishimura, T. Saito, Y. Yang, T. Kouno,
814 T. Fukutomi, T. Hoshii, A. Hirao, K. Takagi, T. Mizushima, H. Motohashi, M.S. Lee, T.
815 Yoshimori, K. Tanaka, M. Yamamoto, and M. Komatsu. 2013. Phosphorylation of p62 activates
816 the Keap1-Nrf2 pathway during selective autophagy. *Mol Cell*. 51:618-631.
817 Ikeda, R., D. Noshiro, H. Morishita, S. Takada, S. Kageyama, Y. Fujioka, T. Funakoshi, S. Komatsu-
818 Hirota, R. Arai, E. Ryzhii, M. Abe, T. Koga, H. Motohashi, M. Nakao, K. Sakimura, A. Horii, S.
819 Waguri, Y. Ichimura, N.N. Noda, and M. Komatsu. 2023. Phosphorylation of phase-separated
820 p62 bodies by ULK1 activates a redox-independent stress response. *EMBO J*. 42:e113349.
821 Jacomin, A.C., S. Samavedam, V. Promponas, and I.P. Nezis. 2016. iLIR database: A web resource for
822 LIR motif-containing proteins in eukaryotes. *Autophagy*. 12:1945-1953.
823 Johansen, T., and T. Lamark. 2011. Selective autophagy mediated by autophagic adapter proteins.
824 *Autophagy*. 7:279-296.
825 Jumper, J., R. Evans, A. Pritzel, T. Green, M. Figurnov, O. Ronneberger, K. Tunyasuvunakool, R. Bates,
826 A. Zidek, A. Potapenko, A. Bridgland, C. Meyer, S.A.A. Kohl, A.J. Ballard, A. Cowie, B.
827 Romera-Paredes, S. Nikolov, R. Jain, J. Adler, T. Back, S. Petersen, D. Reiman, E. Clancy, M.
828 Zielinski, M. Steinegger, M. Pacholska, T. Berghammer, S. Bodenstein, D. Silver, O. Vinyals,
829 A.W. Senior, K. Kavukcuoglu, P. Kohli, and D. Hassabis. 2021. Highly accurate protein structure
830 prediction with AlphaFold. *Nature*. 596:583-589.
831 Kalaria, R.N. 2016. Neuropathological diagnosis of vascular cognitive impairment and vascular dementia
832 with implications for Alzheimer's disease. *Acta Neuropathol*. 131:659-685.
833 Kalvari, I., S. Tsompanis, N.C. Mulakkal, R. Osgood, T. Johansen, I.P. Nezis, and V.J. Promponas. 2014.
834 iLIR: A web resource for prediction of Atg8-family interacting proteins. *Autophagy*. 10:913-925.
835 Kelley, L.A., S. Mezulis, C.M. Yates, M.N. Wass, and M.J. Sternberg. 2015. The Phyre2 web portal for
836 protein modeling, prediction and analysis. *Nat Protoc*. 10:845-858.
837 Kim, K.A., D. Shin, J.H. Kim, Y.J. Shin, G.K. Rajanikant, A. Majid, S.H. Baek, and O.N. Bae. 2018.
838 Role of Autophagy in Endothelial Damage and Blood-Brain Barrier Disruption in Ischemic
839 Stroke. *Stroke*. 49:1571-1579.
840 Kimura, T., M. Mandell, and V. Deretic. 2016. Precision autophagy directed by receptor regulators -
841 emerging examples within the TRIM family. *J Cell Sci*. 129:881-891.
842 Klionsky, D.J., A.K. Abdel-Aziz, S. Abdelfatah, M. Abdellatif, A. Abdoli, S. Abel, H. Abeliovich, M.H.
843 Abildgaard, Y.P. Abudu, A. Acevedo-Arozena, I.E. Adamopoulos, K. Adeli, T.E. Adolph, A.
844 Adornetto, E. Aflaki, G. Agam, A. Agarwal, B.B. Aggarwal, M. Agnello, P. Agostinis, J.N.
845 Agrewala, A. Agrotis, P.V. Aguilar, S.T. Ahmad, Z.M. Ahmed, U. Ahumada-Castro, S. Aits, S.
846 Aizawa, Y. Akkoc, T. Akoumianaki, H.A. Akpinar, A.M. Al-Abd, L. Al-Akra, A. Al-Gharaibeh,
847 M.A. Alaoui-Jamali, S. Alberti, E. Alcocer-Gomez, C. Alessandri, M. Ali, M.A. Alim Al-Bari, S.
848 Aliwaini, J. Alizadeh, E. Almacellas, A. Almasan, A. Alonso, G.D. Alonso, N. Altan-Bonnet,
849 D.C. Altieri, E.M.C. Alvarez, S. Alves, C. Alves da Costa, M.M. Alzaharna, M. Amadio, C.
850 Amantini, C. Amaral, S. Ambrosio, A.O. Amer, V. Ammanathan, Z. An, S.U. Andersen, S.A.
851 Andrabi, M. Andrade-Silva, A.M. Andres, S. Angelini, D. Ann, U.C. Anozie, M.Y. Ansari, P.

852 Antas, A. Antebi, Z. Anton, T. Anwar, L. Apetoh, N. Apostolova, T. Araki, Y. Araki, K. Arasaki,
853 W.L. Araujo, J. Araya, C. Arden, M.A. Arevalo, S. Arguelles, E. Arias, J. Arikkath, H. Arimoto,
854 A.R. Ariosa, D. Armstrong-James, L. Arnaune-Pelloquin, A. Aroca, D.S. Arroyo, I. Arsov, R.
855 Artero, D.M.L. Asaro, M. Aschner, M. Ashrafizadeh, O. Ashur-Fabian, A.G. Atanasov, A.K. Au,
856 P. Auberger, H.W. Auner, L. Aurelian, et al. 2021. Guidelines for the use and interpretation of
857 assays for monitoring autophagy (4th edition)(1). *Autophagy*. 17:1-382.
858 Koliopoulos, M.G., D. Esposito, E. Christodoulou, I.A. Taylor, and K. Rittinger. 2016. Functional role of
859 TRIM E3 ligase oligomerization and regulation of catalytic activity. *EMBO J*. 35:1204-1218.
860 Koliopoulos, M.G., M. Lethier, A.G. van der Veen, K. Haubrich, J. Hennig, E. Kowalinski, R.V. Stevens,
861 S.R. Martin, C. Reis e Sousa, S. Cusack, and K. Rittinger. 2018. Molecular mechanism of
862 influenza A NS1-mediated TRIM25 recognition and inhibition. *Nat Commun*. 9:1820.
863 Kozakov, D., D.R. Hall, B. Xia, K.A. Porter, D. Padhorny, C. Yueh, D. Beglov, and S. Vajda. 2017. The
864 ClusPro web server for protein-protein docking. *Nat Protoc*. 12:255-278.
865 Ma, P., M. Schwarten, L. Schneider, A. Boeske, N. Henke, D. Lisak, S. Weber, J. Mohrluder, M. Stoldt,
866 B. Strodel, A. Methner, S. Hoffmann, O.H. Weiergraber, and D. Willbold. 2013. Interaction of
867 Bcl-2 with the autophagy-related GABAA receptor-associated protein (GABARAP): biophysical
868 characterization and functional implications. *J Biol Chem*. 288:37204-37215.
869 Mahi, N.A., M.F. Najafabadi, M. Pilarczyk, M. Kouril, and M. Medvedovic. 2019. GREIN: An
870 Interactive Web Platform for Re-analyzing GEO RNA-seq Data. *Sci Rep*. 9:7580.
871 Maillard, P., S. Seshadri, A. Beiser, J.J. Himali, R. Au, E. Fletcher, O. Carmichael, P.A. Wolf, and C.
872 DeCarli. 2012. Effects of systolic blood pressure on white-matter integrity in young adults in the
873 Framingham Heart Study: a cross-sectional study. *Lancet Neurol*. 11:1039-1047.
874 Majolee, J., I. Kovacevic, and P.L. Hordijk. 2019. Ubiquitin-based modifications in endothelial cell-cell
875 contact and inflammation. *J Cell Sci*. 132.
876 Mandell, M.A., A. Jain, J. Arko-Mensah, S. Chauhan, T. Kimura, C. Dinkins, G. Silvestri, J. Munch, F.
877 Kirchhoff, A. Simonsen, Y. Wei, B. Levine, T. Johansen, and V. Deretic. 2014. TRIM proteins
878 regulate autophagy and can target autophagic substrates by direct recognition. *Dev Cell*. 30:394-
879 409.
880 McQuin, C., A. Goodman, V. Chernyshev, L. Kamentsky, B.A. Cimini, K.W. Karhohs, M. Doan, L.
881 Ding, S.M. Rafelski, D. Thirstrup, W. Wiegraebe, S. Singh, T. Becker, J.C. Caicedo, and A.E.
882 Carpenter. 2018. CellProfiler 3.0: Next-generation image processing for biology. *PLoS Biol*.
883 16:e2005970.
884 Meng, Q., L. Pu, M. Qi, S. Li, B. Sun, Y. Wang, B. Liu, and F. Li. 2022. Laminar shear stress inhibits
885 inflammation by activating autophagy in human aortic endothelial cells through HMGB1 nuclear
886 translocation. *Commun Biol*. 5:425.
887 Mi, H., A. Muruganujan, D. Ebert, X. Huang, and P.D. Thomas. 2019. PANTHER version 14: more
888 genomes, a new PANTHER GO-slim and improvements in enrichment analysis tools. *Nucleic*
889 *Acids Res*. 47:D419-D426.
890 Mishra, A., C. Duplaa, D. Vojinovic, H. Suzuki, M. Sargurupremraj, N.R. Zilhao, S. Li, T.M. Bartz, X.
891 Jian, W. Zhao, E. Hofer, K. Wittfeld, S.E. Harris, S. van der Auwera-Palitschka, M. Luciano, J.C.
892 Bis, H.H.H. Adams, C.L. Satizabal, R.F. Gottesman, P.G. Gampawar, R. Bulow, S. Weiss, M.
893 Yu, M.E. Bastin, O.L. Lopez, M.W. Vernooij, A.S. Beiser, U. Volker, T. Kacprowski, A.
894 Soumare, J.A. Smith, D.S. Knopman, Z. Morris, Y. Zhu, J.I. Rotter, C. Dufouil, M. Valdes
895 Hernandez, S. Munoz Maniega, M. Lathrop, E. Boerwinkle, R. Schmidt, M. Ihara, B. Mazoyer,
896 Q. Yang, A. Joutel, E. Tournier-Lasserve, L.J. Launer, I.J. Deary, T.H. Mosley, P. Amouyel, C.S.
897 DeCarli, B.M. Psaty, C. Tzourio, S.L.R. Kardia, H.J. Grabe, A. Teumer, C.M. van Duijn, H.
898 Schmidt, J.M. Wardlaw, M.A. Ikram, M. Fornage, V. Gudnason, S. Seshadri, P.M. Matthews,
899 W.T. Longstreth, T. Couffinhal, and S. Debette. 2022. Gene-mapping study of extremes of
900 cerebral small vessel disease reveals TRIM47 as a strong candidate. *Brain*. 145:1992-2007.

901 Mok, K.K., S.H. Yeung, G.W. Cheng, I.W. Ma, R.H. Lee, K. Herrup, and K.H. Tse. 2023.
902 Apolipoprotein E epsilon4 disrupts oligodendrocyte differentiation by interfering with astrocyte-
903 derived lipid transport. *J Neurochem*. 165:55-75.
904 Montagne, A., A.M. Nikolakopoulou, Z. Zhao, A.P. Sagare, G. Si, D. Lazic, S.R. Barnes, M. Daianu, A.
905 Ramanathan, A. Go, E.J. Lawson, Y. Wang, W.J. Mack, P.M. Thompson, J.A. Schneider, J.
906 Varkey, R. Langen, E. Mullins, R.E. Jacobs, and B.V. Zlokovic. 2018. Pericyte degeneration
907 causes white matter dysfunction in the mouse central nervous system. *Nat Med*. 24:326-337.
908 Montesano, R., M.S. Pepper, U. Mohle-Steinlein, W. Risau, E.F. Wagner, and L. Orci. 1990. Increased
909 proteolytic activity is responsible for the aberrant morphogenetic behavior of endothelial cells
910 expressing the middle T oncogene. *Cell*. 62:435-445.
911 Nussenzweig, S.C., S. Verma, and T. Finkel. 2015. The role of autophagy in vascular biology. *Circ Res*.
912 116:480-488.
913 Pan, X., Y. Chen, Y. Shen, and J. Tantai. 2019. Knockdown of TRIM65 inhibits autophagy and cisplatin
914 resistance in A549/DDP cells by regulating miR-138-5p/ATG7. *Cell Death Dis*. 10:429.
915 Persyn, E., K.B. Hanscombe, J.M.M. Howson, C.M. Lewis, M. Traylor, and H.S. Markus. 2020.
916 Genome-wide association study of MRI markers of cerebral small vessel disease in 42,310
917 participants. *Nat Commun*. 11:2175.
918 Pineda, C.T., S. Ramanathan, K. Fon Tacer, J.L. Weon, M.B. Potts, Y.H. Ou, M.A. White, and P.R. Potts.
919 2015. Degradation of AMPK by a cancer-specific ubiquitin ligase. *Cell*. 160:715-728.
920 Pires, P.W., C.M. Dams Ramos, N. Matin, and A.M. Dorrance. 2013. The effects of hypertension on the
921 cerebral circulation. *Am J Physiol Heart Circ Physiol*. 304:H1598-1614.
922 Prins, N.D., and P. Scheltens. 2015. White matter hyperintensities, cognitive impairment and dementia:
923 an update. *Nat Rev Neurol*. 11:157-165.
924 Qian, Y., Z. Wang, H. Lin, T. Lei, Z. Zhou, W. Huang, X. Wu, L. Zuo, J. Wu, Y. Liu, L.F. Wang, X.H.
925 Guan, K.Y. Deng, M. Fu, and H.B. Xin. 2022. TRIM47 is a novel endothelial activation factor
926 that aggravates lipopolysaccharide-induced acute lung injury in mice via K63-linked
927 ubiquitination of TRAF2. *Signal Transduct Target Ther*. 7:148.
928 Rodor, J., S.H. Chen, J.P. Scanlon, J.P. Monteiro, A. Caudrillier, S. Sweta, K.R. Stewart, A. Shmakova,
929 R. Dobie, B.E.P. Henderson, K. Stewart, P.W.F. Hadoke, M. Southwood, S.D. Moore, P.D.
930 Upton, N.W. Morrell, Z. Li, S.Y. Chan, A. Handen, R. Lafyatis, L. de Rooij, N.C. Henderson, P.
931 Carmeliet, A.M. Spiroski, M. Brittan, and A.H. Baker. 2022. Single-cell RNA sequencing
932 profiling of mouse endothelial cells in response to pulmonary arterial hypertension. *Cardiovasc*
933 *Res*. 118:2519-2534.
934 Roseborough, A.D., L. Saad, M. Goodman, L.E. Cipriano, V.C. Hachinski, and S.N. Whitehead. 2023.
935 White matter hyperintensities and longitudinal cognitive decline in cognitively normal
936 populations and across diagnostic categories: A meta-analysis, systematic review, and
937 recommendations for future study harmonization. *Alzheimers Dement*. 19:194-207.
938 Russell, A.J.C., J.A. Weir, N.M. Nadaf, M. Shabet, V. Kumar, S. Kambhampati, R. Raichur, G.J.
939 Marrero, S. Liu, K.S. Balderrama, C.R. Vanderburg, V. Shanmugam, L. Tian, C.J. Wu, C.H.
940 Yoon, E.Z. Macosko, and F. Chen. 2023. Slide-tags: scalable, single-nucleus barcoding for multi-
941 modal spatial genomics. *bioRxiv*.
942 Sanchez, J.G., K. Okreglicka, V. Chandrasekaran, J.M. Welker, W.I. Sundquist, and O. Pornillos. 2014.
943 The tripartite motif coiled-coil is an elongated antiparallel hairpin dimer. *Proc Natl Acad Sci U S*
944 *A*. 111:2494-2499.
945 Sargurupremraj, M., H. Suzuki, X. Jian, C. Sarnowski, T.E. Evans, J.C. Bis, G. Eiriksdottir, S. Sakaue, N.
946 Terzikhan, M. Habes, W. Zhao, N.J. Armstrong, E. Hofer, L.R. Yanek, S.P. Hagenaars, R.B.
947 Kumar, E.B. van den Akker, R.E. McWhirter, S. Trompet, A. Mishra, Y. Saba, C.L. Satizabal, G.
948 Beaudet, L. Petit, A. Tsuchida, L. Zago, S. Schilling, S. Sigurdsson, R.F. Gottesman, C.E. Lewis,
949 N.T. Aggarwal, O.L. Lopez, J.A. Smith, M.C. Valdes Hernandez, J. van der Grond, M.J. Wright,
950 M.J. Knol, M. Dorr, R.J. Thomson, C. Bordes, Q. Le Grand, M.G. Duperron, A.V. Smith, D.S.
951 Knopman, P.J. Schreiner, D.A. Evans, J.I. Rotter, A.S. Beiser, S.M. Maniega, M. Beekman, J.

952 Trollor, D.J. Stott, M.W. Vernooij, K. Wittfeld, W.J. Niessen, A. Soumare, E. Boerwinkle, S.
953 Sidney, S.T. Turner, G. Davies, A. Thalamuthu, U. Volker, M.A. van Buchem, R.N. Bryan, J.
954 Dupuis, M.E. Bastin, D. Ames, A. Teumer, P. Amouyel, J.B. Kwok, R. Bulow, I.J. Deary, P.R.
955 Schofield, H. Brodaty, J. Jiang, Y. Tabara, K. Setoh, S. Miyamoto, K. Yoshida, M. Nagata, Y.
956 Kamatani, F. Matsuda, B.M. Psaty, D.A. Bennett, P.L. De Jager, T.H. Mosley, P.S. Sachdev, R.
957 Schmidt, H.R. Warren, E. Evangelou, D.A. Tregouet, C. International Network against
958 Thrombosis, C. International Headache Genomics, M.A. Ikram, W. Wen, C. DeCarli, V.K.
959 Srikanth, J.W. Jukema, E.P. Slagboom, S.L.R. Kardia, et al. 2020. Cerebral small vessel disease
960 genomics and its implications across the lifespan. *Nat Commun*. 11:6285.
961 Sarnowski, C., C.L. Satizabal, C. DeCarli, A.N. Pitsillides, L.A. Cupples, R.S. Vasan, J.G. Wilson, J.C.
962 Bis, M. Fornage, A.S. Beiser, A.L. DeStefano, J. Dupuis, S. Seshadri, N.T.-O.f.P.M. Consortium,
963 and T.O.N.W. Group. 2018. Whole genome sequence analyses of brain imaging measures in the
964 Framingham Study. *Neurology*. 90:e188-e196.
965 Saunders, A., E.Z. Macosko, A. Wysoker, M. Goldman, F.M. Krienen, H. de Rivera, E. Bien, M. Baum,
966 L. Bortolin, S. Wang, A. Goeva, J. Nemesh, N. Kamitaki, S. Brumbaugh, D. Kulp, and S.A.
967 McCarroll. 2018. Molecular Diversity and Specializations among the Cells of the Adult Mouse
968 Brain. *Cell*. 174:1015-1030 e1016.
969 Shim, Y.S., D.W. Yang, C.M. Roe, M.A. Coats, T.L. Benzinger, C. Xiong, J.E. Galvin, N.J. Cairns, and
970 J.C. Morris. 2015. Pathological correlates of white matter hyperintensities on magnetic resonance
971 imaging. *Dement Geriatr Cogn Disord*. 39:92-104.
972 Spandidos, A., X. Wang, H. Wang, and B. Seed. 2010. PrimerBank: a resource of human and mouse PCR
973 primer pairs for gene expression detection and quantification. *Nucleic Acids Res*. 38:D792-799.
974 Takase, H., G. Hamanaka, R. Ohtomo, H. Ishikawa, K.K. Chung, E.T. Mandeville, J. Lok, M. Fornage,
975 K. Herrup, K.H. Tse, E.H. Lo, and K. Arai. 2021. Transcriptome Profiling of Mouse Corpus
976 Callosum After Cerebral Hypoperfusion. *Front Cell Dev Biol*. 9:685261.
977 Traylor, M., D.J. Tozer, I.D. Croall, D.M. Lisiecka Ford, A.O. Olorunda, G. Boncoraglio, M. Dichgans,
978 R. Lemmens, J. Rosand, N.S. Rost, P.M. Rothwell, C.L.M. Sudlow, V. Thijs, L. Rutten-Jacobs,
979 H.S. Markus, and C. International Stroke Genetics. 2019. Genetic variation in PLEKHG1 is
980 associated with white matter hyperintensities (n = 11,226). *Neurology*. 92:e749-e757.
981 Tse, K.H., and K. Herrup. 2017. Re-imagining Alzheimer's disease - the diminishing importance of
982 amyloid and a glimpse of what lies ahead. *J Neurochem*. 143:432-444.
983 Vergoossen, L.W.M., J.F.A. Jansen, T.T. van Sloten, C.D.A. Stehouwer, N.C. Schaper, A. Wesselius,
984 P.C. Dagnelie, S. Kohler, M.P.J. van Boxtel, A.A. Kroon, J.J.A. de Jong, M.T. Schram, and W.H.
985 Backes. 2021. Interplay of White Matter Hyperintensities, Cerebral Networks, and Cognitive
986 Function in an Adult Population: Diffusion-Tensor Imaging in the Maastricht Study. *Radiology*.
987 298:384-392.
988 Verhaaren, B.F., S. Debette, J.C. Bis, J.A. Smith, M.K. Ikram, H.H. Adams, A.H. Beecham, K.B. Rajan,
989 L.M. Lopez, S. Barral, M.A. van Buchem, J. van der Grond, A.V. Smith, K. Hegenscheid, N.T.
990 Aggarwal, M. de Andrade, E.J. Atkinson, M. Beekman, A.S. Beiser, S.H. Blanton, E.
991 Boerwinkle, A.M. Brickman, R.N. Bryan, G. Chauhan, C.P. Chen, V. Chouraki, A.J. de Craen, F.
992 Crivello, I.J. Deary, J. Deelen, P.L. De Jager, C. Dufouil, M.S. Elkind, D.A. Evans, P.
993 Freudenberger, R.F. Gottesman, V. Guethnason, M. Habes, S.R. Heckbert, G. Heiss, S. Hilal, E.
994 Hofer, A. Hofman, C.A. Ibrahim-Verbaas, D.S. Knopman, C.E. Lewis, J. Liao, D.C. Liewald, M.
995 Luciano, A. van der Lugt, O.O. Martinez, R. Mayeux, B. Mazoyer, M. Nalls, M. Nauck, W.J.
996 Niessen, B.A. Oostra, B.M. Psaty, K.M. Rice, J.I. Rotter, B. von Sarnowski, H. Schmidt, P.J.
997 Schreiner, M. Schuur, S.S. Sidney, S. Sigurdsson, P.E. Slagboom, D.J. Stott, J.C. van Swieten, A.
998 Teumer, A.M. Toglhofer, M. Traylor, S. Trompet, S.T. Turner, C. Tzourio, H.W. Uh, A.G.
999 Uitterlinden, M.W. Vernooij, J.J. Wang, T.Y. Wong, J.M. Wardlaw, B.G. Windham, K. Wittfeld,
1000 C. Wolf, C.B. Wright, Q. Yang, W. Zhao, A. Zijdenbos, J.W. Jukema, R.L. Sacco, S.L. Kardia, P.
1001 Amouyel, T.H. Mosley, W.T. Longstreth, Jr., C.C. DeCarli, C.M. van Duijn, R. Schmidt, L.J.

1002 Launer, H.J. Grabe, S.S. Seshadri, et al. 2015. Multiethnic genome-wide association study of
1003 cerebral white matter hyperintensities on MRI. *Circ Cardiovasc Genet*. 8:398-409.
1004 Verhaaren, B.F., M.W. Vernooij, R. de Boer, A. Hofman, W.J. Niessen, A. van der Lugt, and M.A.
1005 Ikram. 2013. High blood pressure and cerebral white matter lesion progression in the general
1006 population. *Hypertension*. 61:1354-1359.
1007 Vion, A.C., M. Kheloufi, A. Hammoutene, J. Poisson, J. Lasselin, C. Devue, I. Pic, N. Dupont, J. Busse,
1008 K. Stark, J. Lafaurie-Janvore, A.I. Barakat, X. Loyer, M. Souyri, B. Viollet, P. Julia, A. Tedgui,
1009 P. Codogno, C.M. Boulanger, and P.E. Rautou. 2017. Autophagy is required for endothelial cell
1010 alignment and atheroprotection under physiological blood flow. *Proc Natl Acad Sci U S A*.
1011 114:E8675-E8684.
1012 Wang, W., Z. Xia, J.C. Farre, and S. Subramani. 2018. TRIM37 deficiency induces autophagy through
1013 deregulating the MTORC1-TFEB axis. *Autophagy*. 14:1574-1585.
1014 Wegner, S., R. Uhlemann, V. Boujon, B. Ersoy, M. Endres, G. Kronenberg, and K. Gertz. 2020.
1015 Endothelial Cell-Specific Transcriptome Reveals Signature of Chronic Stress Related to Worse
1016 Outcome After Mild Transient Brain Ischemia in Mice. *Mol Neurobiol*. 57:1446-1458.
1017 Wirth, M., W. Zhang, M. Razi, L. Nyoni, D. Joshi, N. O'Reilly, T. Johansen, S.A. Tooze, and S.
1018 Mouilleron. 2019. Molecular determinants regulating selective binding of autophagy adapters and
1019 receptors to ATG8 proteins. *Nat Commun*. 10:2055.
1020 Wu, F., B. Han, S. Wu, L. Yang, S. Leng, M. Li, J. Liao, G. Wang, Q. Ye, Y. Zhang, H. Chen, X. Chen,
1021 M. Zhong, Y. Xu, Q. Liu, J.H. Zhang, and H. Yao. 2019. Circular RNA TLK1 Aggravates
1022 Neuronal Injury and Neurological Deficits after Ischemic Stroke via miR-335-3p/TIPARP. *J*
1023 *Neurosci*. 39:7369-7393.
1024 Wu, Y.T., H.L. Tan, G. Shui, C. Bauvy, Q. Huang, M.R. Wenk, C.N. Ong, P. Codogno, and H.M. Shen.
1025 2010. Dual role of 3-methyladenine in modulation of autophagy via different temporal patterns of
1026 inhibition on class I and III phosphoinositide 3-kinase. *J Biol Chem*. 285:10850-10861.
1027 Ximerakis, M., S.L. Lipnick, B.T. Innes, S.K. Simmons, X. Adiconis, D. Dionne, B.A. Mayweather, L.
1028 Nguyen, Z. Niziolek, C. Ozek, V.L. Butty, R. Isserlin, S.M. Buchanan, S.S. Levine, A. Regev,
1029 G.D. Bader, J.Z. Levin, and L.L. Rubin. 2019. Single-cell transcriptomic profiling of the aging
1030 mouse brain. *Nat Neurosci*. 22:1696-1708.
1031 Zhao, Z., A.R. Nelson, C. Betsholtz, and B.V. Zlokovic. 2015. Establishment and Dysfunction of the
1032 Blood-Brain Barrier. *Cell*. 163:1064-1078.
1033

Human

Gene Symbol	NCBI Protein accession	Motif	Start	End	Pattern	PSSM Score	LIR in Anchor
SQSTM1	NP_003891.1	xLIR	336	341	DDWTHL	24	Yes
TRIM47	NP_258411.2	WxxL	379	384	NQWEQL	14	Yes
TRIM28	AAH04978.1	WxxL	515	520	EDYNLI	13	Yes
TRIM63	NP_115977.2	WxxL	305	310	MDFFTL	10	Yes
TRIM41	NP_291027.3	WxxL	315	320	SEFGRL	7	Yes
TRIM20	NP_000234.1	xLIR	523	528	SEWELL	20	No
TRIM13	NP_998755.1	WxxL	284	289	SQWEDI	17	No
TRIM21	NP_003132.2	WxxL	9	14	MMWEEV	16	No
TRIM25	NP_005073.2	xLIR	303	308	DEFEFL	16	No
TRIM49	NP_065091.1	WxxL	41	46	LNWQDI	15	No
TRIM5	NP_001397887.1	WxxL	183	188	ADFEQL	14	No
TRIM6	NP_001003818.1	WxxL	326	331	SYWVDV	14	No
TRIM50	NP_835226.2	xLIR	177	182	REFQEL	13	No
TRIM22	NP_006065.2	WxxL	173	178	KNYIQI	9	No
TRIM55	NP_908973.1	WxxL	213	218	EKFDYL	9	No
TRIM65	NP_775818.2	xLIR	333	338	LTFDPV	9	No
TRIM17	NP_001020111.1	WxxL	401	406	STFSAL	9	No
TRIM40	NP_001273562.1	WxxL	238	243	VIYPQL	0	No

Mouse

Gene Symbol	NCBI Protein accession	Motif	Start	End	Pattern	PSSM Score	LIR in Anchor
Sqstm1	NP_035148.1	xLIR	338	343	DDWTHL	24	Yes
Trim28	EDL38082.1	WxxL	515	520	EDYNLI	13	Yes
Trim63	NP_001034137.2	WxxL	305	310	MDYFTL	11	Yes
Trim20	XP_006522424.1	WxxL	227	232	EVYVYL	8	Yes
Trim41	NP_663352.2	WxxL	315	320	SEFGRL	7	Yes
Trim21	NP_001076021.1	xLIR	5	10	KMWEEV	18	No
Trim47	NP_001192010.1	WxxL	383	388	SQWEQL	16	No
Trim25	NP_033572.2	xLIR	302	307	DEFEFL	16	No
Trim6	NP_001013637.1	WxxL	298	303	SYWVDV	14	No
Trim5	NP_001297531.1	WxxL	296	301	RYWVQV	13	No
Trim50	NP_839971.1	xLIR	177	182	REFQEL	13	No
Trim13	NP_001157692.1	WxxL	284	289	SQWGDI	12	No
Trim17	NP_112449.1	xLIR	187	192	EEFQKV	11	No
Trim55	NP_001074750.1	WxxL	213	218	EKFDHL	10	No
Trm65	NP_848917.2	WxxL	344	349	NQYLHL	8	No
Trim40	NP_001028407.1	WxxL	170	175	LPWHWL	7	No

Table 1. Screening of LIR (LC3-interacting region)-motif among known autophagy-associated TRIM family members in human and mouse

PSSM: position-specific scoring matrix score; LIR = WxxL or xLIR; **W**xx**L**, LIR consensus sequence where x can be any amino acid among the four residues; xLIR, LIR consensus sequence where the six residues can be any amino acids as follow (ADEFGLPRSK)(DEGMSTV)(**WFY**)(DEILQTV)(ADEFHIKLMPSTV)(**ILV**). SQSTM encodes Sequestosome 1(or p62) which is a verified LC3 interacting substrate and serves as the positive control.